A DETAILED COMPARISON OF HYDROGEN
AND MERCURY EMBRITTLEMENT
IN MONEL 400

By

ROBERT STEPHEN FREDELL

Bachelor of Science

Oklahoma State University

Stillwater, Oklahoma

1982

Submitted to the Faculty of the Graduate College
of the Oklahoma State University
in partial fulfillment of the requirements
for the Degree of
MASTER OF SCIENCE
December, 1983

A DETAILED COMPARISON OF HYDROGEN AND MERCURY EMBRITTLEMENT IN MONEL 400

Thesis Approved:

C E Price
Thesis Adviser

James K. Good

Richard L. Lowery

Norman N Durham
Dean of the Graduate College

ACKNOWLEDGMENTS

I would like to express my appreciation to those who have helped during this study. Special thanks go to Dr. C. E. Price, my major adviser, for his guidance and encouragement throughout my studies at Oklahoma State University. He was always willing to discuss a problem or to brood on the more weighty questions which arise during the writing of a thesis. My thanks go also to Dr. Richard Lowery and Dr. Keith Good for serving on my committee.

I would also like to thank Dr. Keith Good and Mr. Leland Traylor for beginning this series of studies on the embrittlement of nickel alloys, and Mr. James Morris for his helpful advice and willing ear.

The School of Mechanical Engineering is gratefully acknowledged for funding a portion of my research. Finally, I would like to thank the Air Force Institute of Technology for making my graduate study possible.

TABLE OF CONTENTS

Chapter Page

I. INTRODUCTION 1

II. REVIEW OF THE LITERATURE 3

Introduction 3
Embrittlement by Liquid Metals 3
Embrittlement by Hydrogen 9
The Effect of Metallurgical Variables on Embrittlement 10

III. EXPERIMENTAL PROCEDURE 12

The Material 12
Testing 15
Microscopic Observations 16

IV. EXPERIMENTAL RESULTS 20

Variation in Strain Rate 20
Variation in Grain Size 49
Fatigue Tests 67
Discussion 76

V. CONCLUSIONS 88

A SELECTED BIBLIOGRAPHY 90

LIST OF TABLES

Table Page

I. Composition and As-Received Properties of Monel 400 Huntington Alloy, Heat Number M9631B 15

II. Tensile Strength and Reduction in Area of Monel 400 Tested in Air 21

III. Tensile Strength and Reduction in Area of Monel 400 Tested in Mercury 21

IV. Extent of Side Cracking in Monel 400 Tested in Mercury 24

V. Results of Static/Tensile Tests of Monel 400 in Mercury 37

VI. Tensile Strength and Reduction in Area of Monel 400 Tested in Hydrogen 39

VII. Extent of Side Cracking in Monel 400 Tested in Hydrogen 39

VIII. Effect of Sample Diameter on Monel 400 Tested in Hydrogen 49

IX. Variation of Tensile Strength and Reduction in Area With Grain Size of Monel 400 Tested in Air 50

X. Variation of Tensile Strength and Reduction in Area With Grain Size of Monel 400 Tested in Mercury 51

XI. Variation of the Extent of Side Cracking With Grain Size of Monel 400 Tested in Mercury 51

XII. Variation of Tensile Strength and Reduction in Area With Grain Size of Monel 400 Tested in Hydrogen 62

XIII. Variation of the Extent of Side Cracking With Grain Size of Monel 400 Tested in Hydrogen 62

Table Page

XIV. Fatigue Life Data for Fine-Grained Monel 400 Tested in Air, Hydrogen, and Mercury 72

XV. Fatigue Life Data for 250 μm Grain Size Monel 400 Tested in Air, Hydrogen, and Mercury 73

LIST OF FIGURES

Figure Page

1. Schematic Representation of Displacement of Atoms at the Tip of a Crack 6

2. Specimen Geometry for Embrittlement Testing 14

3. Environmental Cell Used in Hydrogen Testing 18

4. Fracture Surface of Monel 400 Broken in Air 23

5. Detail of Microvoids Covering the Surface of Monel 400 Broken in Air 23

6. Fracture Surface of Monel 400 Broken in Mercury at 1.6×10^{-2} s^{-1} 27

7. Fracture Surface of Monel 400 Broken in Mercury at 1.6×10^{-3} s^{-1} 27

8. Fracture Surface of Monel 400 Broken in Mercury at 1.6×10^{-4} s^{-1} 29

9. Fracture Surface of Monel 400 Broken in Mercury at 1.6×10^{-5} s^{-1} 29

10. Fracture Surface of Monel 400 Broken in Mercury at 1.6×10^{-6} s^{-1} 31

11. Detail of Transgranular Tearing at Lower Edge of Figure 6 31

12. Appearance of Intergranular Cracking and Light Tearing Near the Center of Figure 7 33

13. Intergranular Cracking Near the Center of Figure 8 33

14. Clean Intergranular Cracking at the Center of Figure 9 36

15. Utterly Clean Intergranular Cracking at the Center of Figure 10 36

Figure Page

16. Fracture Surface of Monel 400 Broken in Hydrogen at 1.6 x 10^{-4} s^{-1} 41

17. Fracture Surface of Monel 400 Broken in Hydrogen at 1.6 x 10^{-5} s^{-1} 41

18. Fracture Surface of Monel 400 Broken in Hydrogen at 1.6 x 10^{-6} s^{-1} 44

19. Rapid Transition of Fracture Mode at the Edge of Figure 16 44

20. Mixed Intergranular and Transgranular Zone at the Edge of Figure 17 46

21. Mixed Intergranular and Transgranular Zone at the Edge of Figure 18 46

22. Tearing, Cracks, and Microvoids at the Center of Figure 17 48

23. Tearing and Cracks Near the Center of Figure 18 48

24. Fracture Surface of 35 μm Grain Size Monel 400 Broken in Mercury 54

25. Fracture Surface of 80 μm Grain Size Monel 400 Broken in Mercury 54

26. Fracture Surface of 150 μm Grain Size Monel 400 Broken in Mercury 56

27. Fracture Surface of 250 μm Grain Size Monel 400 Broken in Mercury 56

28. Fracture Surface of 500 μm Grain Size Monel 400 Broken in Mercury 58

29. Intergranular Cracking Mixed With Tearing at the Edge of Figure 25 58

30. Intergranular Cracking in the Interior of Figure 25 60

31. Transgranular Tearing at the Center of Figure 28 60

32. Fracture Surface of 35 μm Grain Size Monel 400 Broken in Hydrogen 64

33. Fracture Surface of 80 μm Grain Size Monel 400 Broken in Hydrogen 64

Figure Page

34. Fracture Surface of 150 μm Grain Size Monel 400 Broken in Hydrogen 66

35. Fracture Surface of 500 μm Grain Size Monel 400 Broken in Hydrogen 66

36. Intergranular Cracking Covering the Edge of Figure 32 69

37. Relatively Clean Intergranular Cracking Near the Edge of Figure 33 69

38. Tearing and Cracking Near the Edge of Figure 34 71

39. Intergranular-to-Transgranular Transition at the Edge of Figure 35 71

40. Initiation Zone of Fatigue Crack for Test in Mercury 75

41. Small Area of Tearing on Mercury Fatigue Fracture 75

42. Appearance of Fatigue Striations on Mercury Fatigue Fracture 78

43. Initiation Zone of Fatigue Crack for 56 ksi Test in Hydrogen 78

44. Initiation Zone of Fatigue Crack for 53 ksi Test in Hydrogen 80

45. Initiation Zone of Fatigue Crack for 50 ksi Test in Hydrogen 80

CHAPTER I

INTRODUCTION

Embrittlement refers to the loss of ductility and/or tensile strength of an engineering material due to interaction with its environment [1]. Many metals that are normally ductile in inert environments are embrittled by hydrogen and certain specific liquid metals [2]. Embrittlement can cause catastrophic results, for failure can occur in designs supposedly proven to be safe. During the Apollo program, NASA experienced hydrogen embrittlement-related failures of pressure vessels while being filled with gaseous hydrogen to rated pressure [3]. The story is told of catastrophic failures of brass components when ordinary mercury thermometers were broken and their contents spilled on the metal surface [4].

Hydrogen can be introduced into metals while the metal is still in the molten state. Welding and electroplating have been known to cause hydrogen pickup, and cathodic protection of structures can sometimes have the deleterious side effect of inducing hydrogen embrittlement (HE) [5]. In all of the above-mentioned cases, moisture around the pickup site is a common source of hydrogen. Liquid metals, on the other hand, are found in contact with solid metals by design, e.g., liquid-metal-cooled fast breeder reactors [6] and the use of mercury in instruments. Hydrogen embrittlement has a direct economic impact on the petroleum industry, where sour gas (H_2S) is often encountered in deep wells [7]. Temperatures can exceed 400°F, and downhole pressures often reach 20,000 psi. In cases where chemical inhibitors are economically unfeasible, the oil industry often turns to nickel-base alloys to solve its corrosion problems.

This study grew from previous work done at Oklahoma State University. Price and Good [8] tested 10 nickel alloys that typify commercially available Inco alloys, including Nickel 200, the Monels, Inconels, and Incoloys. Testing was done at room temperature in a liquid mercury environment. Good found that all of the alloys tested were susceptible to mercury embrittlement. Traylor [9] tested a similar range of Inco alloys in hydrogen and found they were also embrittled to a degree. The inference was that all nickel alloys, under appropriate conditions, will be embrittled by mercury and hydrogen. Monel 400 and K-500, both of which are used extensively in downhole completions of deep (including sour gas) wells, were found to be the most susceptible to embrittlement of all the alloys that were tested. Researchers [2, 8, 9] have pointed out the similarities in behavior between hydrogen and mercury embrittlement, and have postulated that the embrittling mechanism may be the same for both environments.

Some of the relevant variables affecting embrittlement are strain rate, grain size, and test temperature. The present study is concerned with testing the effects of strain rate and grain size on mercury and hydrogen embrittlement of Monel 400. It is hoped that by comparing the effects of the two environments, a better understanding can be reached of the embrittlement mechanism involved.

CHAPTER II

REVIEW OF THE LITERATURE

Introduction

The present study is a direct follow-up of work done by Traylor [9]; therefore, his review of the literature is directly applicable. Because of this, general background material will not be covered here. The attention of this chapter is focused on pertinent theories of embrittlement mechanisms.

Embrittlement by Liquid Metals

The phenomenon of liquid metal embrittlement (LME) is well documented, but is not yet clearly understood. Consequently, numerous mechanisms have been proposed to explain LME. Four of these models are summarized below.

Reduction in Surface Energy Model

Researchers in both the Soviet Union [10, 11] and the United States [12, 13] have proposed that adsorption of the liquid metal at the solid-liquid metal interface causes a reduction of the free energy at the solid metal surface. This accounts for an effect to a depth of only a few atomic layers, however, and does not provide a large enough reduction in energy to propagate a crack, for it has been shown by Low [14] that the total energy needed for crack propagation is many times greater than the surface energy of the solid. Thus, this model does not seem to account for all of the effects of LME.

Stress-Assisted Dissolution Model

Robertson [15] suggested that crack propagation in LME occurs by dissolution of the stressed atoms at the leading edge of a crack. The dissolved base metal is then diffused into the bulk liquid. He theorized that high stress levels at the crack tip increased the solubility of the base metal in the embrittler. However, researchers [11, 12] have found empirically that embrittlement almost never occurs in two metals which display significant joint solubility. For example, mercury has been shown to embrittle pure nickel, yet the solubility of mercury in nickel is extremely limited. Besides, the dissolution of the base metal would tend to blunt an advancing crack. The conclusion is that the Robertson model is an unlikely mechanism for LME.

Reduction in Cohesion Model

A leading theory advanced by Westwood and Kamdar [16, 17] and Stoloff and Johnston [18] proposes that the liquid metal causes an adsorption-induced reduction in the cohesive strength between base metal atoms (Figure 1). As the sample is stressed, the liquid metal atom B is spontaneously adsorbed at the tip of the crack, reducing the strength of the bond $A-A_o$. When the stress reaches a new (lower) critical breaking stress, the bond breaks and the crack propagates to the bond $A-A_1$, where the sequence begins again. Thus, Kamdar [17] proposes that LME is a special case of brittle fracture, and that the effects of mechanical and

Figure 1. Schematic Representation of Displacement of Atoms at the Tip of a Crack. The bond A-A_o is the crack tip and B is the liquid metal atom. (After Kamdar [17].)

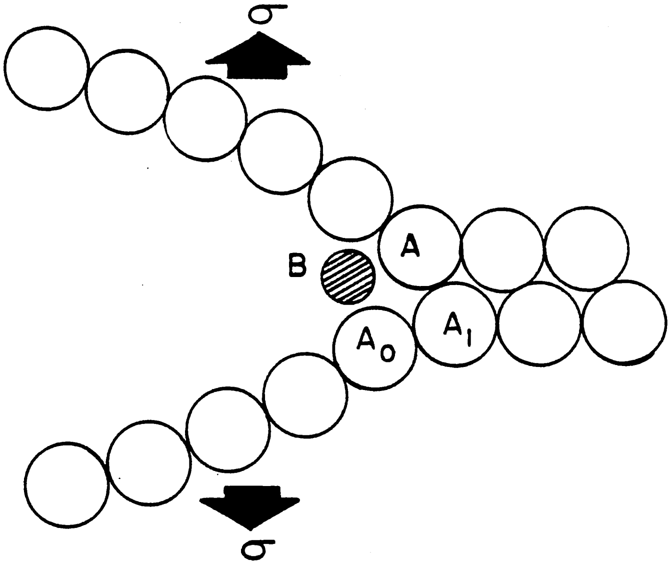
σ
A
B
A_0
A_1
σ

metallurgical factors on embrittlement can be attributed to the principles of brittle fracture.

Gilman [19] and Kelly et al. [20] have presented a criterion by which the ductile or brittle behavior of solids may be predicted. The hypothesis for metals is that if the ratio of the largest tensile fracture stress, σ_{max}, in the neighborhood of the crack tip to the largest shear stress, τ_{max}, on the most favorably-oriented slip plane near the tip is greater than roughly 10, the failure will be predominantly ductile, and if $\sigma_{max}/\tau_{max} \leq 10$, the failure will be largely brittle. σ_{max} and τ_{max} are material properties, and are independent of the state of stress present in the component. The Kelly criterion thus provides a basis for the brittle intergranular fracture of a normally ductile metal when stressed in the presence of an embrittling liquid metal. If adsorption of the liquid metal reduces σ_{max} while leaving τ_{max} unchanged, the ratio σ_{max}/τ_{max} will be reduced, favoring brittle failure. Thus the degree of embrittlement is a function of the reduction of σ_{max}.

For the reduction in the cohesion model to be considered valid, the following effects should be observed for LME:

1. Strain rate effects. Kamdar [17] predicted that an increase in strain rate should increase embrittlement on the basis of an increase of the ductile-to-brittle transition temperature. He based his prediction on tests run on 6 mm square zinc monocrystals coated with liquid gallium and liquid mercury.

2. Grain size effects. In keeping with the "special case of brittle fracture" idea, the fracture strength should vary linearly with $d^{-\frac{1}{2}}$, where d is the material grain size [17]. Specifically, refinement of the grain size decreases embrittlement by decreasing the lengths of dislocation pile-ups.

Stress-Aided Diffusion Penetration Model

Krishtal [21] proposed a mechanism for LME that involved stress-aided diffusion of embrittler atoms into the grain boundaries of the base model. Gordon and An [22], in tests involving indium as an embrittler in 4140 steel, refined the Krishtal idea into a two-step process, whereby (1) the embrittler atoms change from the adsorbed to the dissolved state, and (2) the dissolved embrittler atoms diffuse along grain boundaries. In the penetration zones, the embrittler atoms lower the crack resistance and decrease slip. When enough embrittler atoms have built up to some critical depth in one of the penetration zones, crack nucleation occurs. Thus crack nucleation would occur after some incubation period. The nucleation time, t_n, can be represented by

$$t_n \sim \exp \frac{\Delta G_s}{RT} \exp \frac{\Delta G_d}{RT} , \qquad (1)$$

where ΔG_s and ΔG_d are the respective activation energies for steps (1) and (2). The embrittlement process is thermally activated and stress-dependent.

On the basis of the stress-aided diffusion model, the following characteristics should be expected from LME:

1. Delayed failure should occur after the development of penetration zones.

2. Strain rate effects. Gordon and An [22, p. 458] believe that increasing strain rates require higher temperatures "to provide sufficient volume diffusion to dissipate the grain boundary penetration zones." Therefore, at a constant temperature, increasing the strain rate should decrease embrittlement.

3. Grain size effects. Refining the grain size should decrease the severity of LME by reducing the stress concentrations at dislocation pile-ups at grain boundaries.

Embrittlement by Hydrogen

Many different mechanisms have been suggested to account for hydrogen embrittlement (HE) in metals. Some of these depend on the diffusion of hydrogen into the metal lattice [2]. In nickel and its alloys, though, this volume effect is an unlikely mechanism, for the diffusivity of hydrogen in nickel at 25°C is only $\sim 5 \times 10^{-14}$ m^2/s. Some popular HE theories appear below.

Beachem Hydrogen-Assisted Cracking Model

Beachem [23] suggested that concentrated hydrogen dissolved in the metal lattice just ahead of the crack tip aids in the deformation process by unlocking dislocations and allowing them to move at reduced stresses. In tests on steel, he found a wide range of fractographic features which were dependent upon the stress intensity at the crack tip. At low stress intensities the cracking was intergranular, while at higher stress intensities transgranular tearing and finally microvoids were found. These findings were quite significant in that he showed hydrogen-assisted cracking was not identified with one specific type of fracture surface.

Planar Pressure Mechanism

This model, put forth by Zapffe [24] and Tetelman and Robertson [25], states that the high pressures developed within internal hydrogen gas pores of hydrogen-charged materials cause cracking. This mechanism cannot explain embrittlement of steel by low-pressure hydrogen, for the high pressures simply would not develop within the metal [5].

Reduction of Surface Energy Model

Petch and Stables [26] argued that diffused hydrogen acts to reduce the surface energy at internally free surfaces. As in the similar LME model, this does not provide sufficient reduction in energy to propagate a crack and therefore cannot be considered as the controlling mechanism for HE.

Lynch Adsorption Model

Lynch [2], in research comparing HE and LME in nickel single crystals, proposed that embrittler adsorption at the tip of the advancing crack facilitates the nucleation of dislocations. Crack growth by slip can occur at lower stresses in the presence of an embrittler than in an inert environment, e.g., argon. His mechanism is similar to the Kamdar reduction in cohesion model.

The Effect of Metallurgical Variables on Embrittlement

Costas [27], in tests on nickel-copper alloys that ranged from 10 to 67 percent nickel, found that phosphorus content had a conspicuous effect on the alloys' susceptibility to mercury embrittlement. The amount of phosphorous required to avoid embrittlement increased with increasing nickel content. Heat treatment was also found to have an effect, the implication being that furnace-cooled samples had more phosphorous segregated at the grain boundaries than did quenched samples and were thus better able to resist embrittlement.

Tensile tests on Monel 400 in both mercury and hydrogen environments by Funkenbusch et al. [28] confirmed the earlier work done by Costas [27]. Specimens were either quenched or furnace-cooled from 900°C, and phosphorus concentration at the grain boundaries was found to be twice as high in the furnace-cooled samples. The increased grain boundary concentration decreased embrittlement by both hydrogen and mercury, possibly due to improved grain boundary atomic packing.

CHAPTER III

EXPERIMENTAL PROCEDURE

The Material

Monel 400 (UNS N04400) is a nickel-copper alloy containing 66 percent nickel and 31.5 percent copper nominally. Typical applications of Monel 400 are as pump parts, propeller shafts, chemical-processing equipment, and heat exchanger tubing. The alloy is more resistant than nickel to corrosion under reducing conditions, and more resistant than copper to corrosion under oxidizing conditions. In addition, the alloy is generally free from stress-corrosion cracking. Its face-centered cubic structure affords good ductility and toughness down to liquid helium temperatures, while tensile strengths as high as 120 ksi can be achieved by cold rolling [28]. The as-received Monel 400 was a cold drawn, stress-relieved bar, of 12.7 mm diameter from Huntington Alloy heat number M9631B. The specific chemical composition and mechanical properties are presented in Table I.

Test specimen geometry was the same for both tensile and fatigue tests. Test samples were 130 mm long; ends were unthreaded. The center of the sample had a region approximately 40 mm long in which the diameter gradually decreased to 6.35 mm at the specimen center. Figure 2 shows the specimen geometry. The principle behind the geometry was to localize the fracture zone while avoiding any significant stress concentration.

Figure 2. Specimen Geometry for Embrittlement Testing

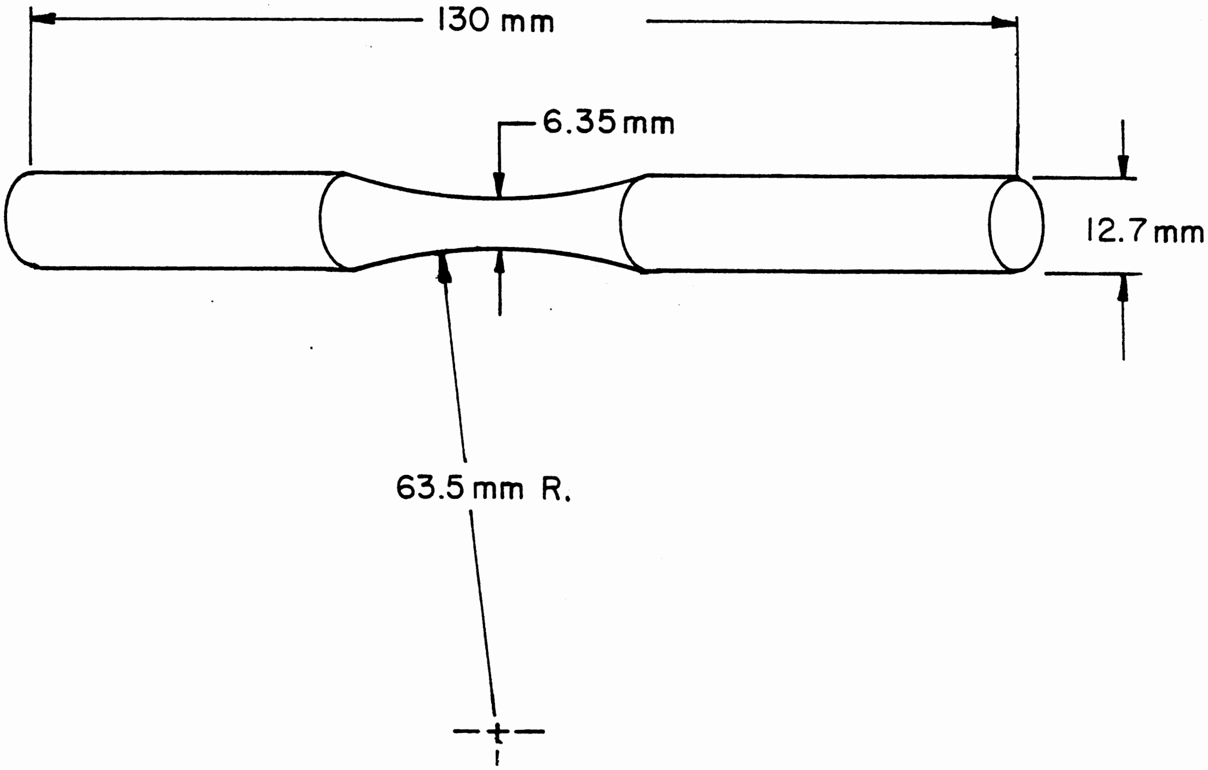
130 mm
6.35 mm
12.7 mm
63.5 mm R.

Tensile specimens typically received a 600 grit finish, although some were chemically polished for surface observations. Fatigue specimens were chemically polished.

TABLE I

COMPOSITION AND AS-RECEIVED PROPERTIES OF MONEL 400
HUNTINGTON ALLOY, HEAT NUMBER M9631B

(A) Chemical Composition Element	Percent	(B) Mechanical Properties	
Nickel	65.710	Yield Strength (0.2% Offset)	97.5 ksi
Copper	31.150	Tensile Strength	117.7 ksi
Iron	1.600	Hardness	R_B 99
Manganese	1.130	% Elongation	25
Silicon	0.230	% Reduction in Area	64
Carbon	0.160		
Aluminum	0.013		
Sulfur	0.009		

Grain size was controlled by annealing in a mild vacuum. Annealing temperatures ranged from 700°C to 1090°C, and as the photographs will show, grain sizes ranged from 25 to over 500 μm. Specimens were furnace-cooled after annealing.

Testing

All tests were performed at room temperature on an MTS machine.

Tensile tests were done under a ramp input; 152 mm in 10^5 s was the typical ramp speed.

Because of specimen geometry, the strain rate at the specimen center had to be measured experimentally. This was done by mounting a 1 mm-long foil-type strain gage on the specimen. The strain gage formed the active gage of a Wheatstone Bridge arrangement. Circuity included a Vishay/Ellis 20 Digital Strain Indicator, with temperature compensation. When the MTS ramp speed was 152 mm in 10^5 s, this arrangement gave a strain rate of 1.6×10^{-5} s^{-1}. Certain tensile tests used ramp speeds of one to three orders of magnitude higher or lower, and are noted in the text. Fatigue tests were run in fluctuating tension ($R = 0$) at approximately 35 Hz, with a sinusoidal loading pattern.

Testing was done in air, mercury, and hydrogen. For the mercury tests, a small cup of mercury surrounded the specimens, which had previously been cleaned in HCl to ensure proper wetting of the specimen by the mercury. For the hydrogen tests, the samples formed the cathode of an electrolytic cell and were dynamically charged at the rate of 200 Am^{-2}. Two platinum wires formed the anode. The electrolyte was sulfuric acid at a pH of 3.2, to which 0.25 g/l of sodium arsenite were added to inhibit hydrogen recombination. Charging was accomplished using a Princeton Applied Research Model 173 Potentiostat/Galvanostat. Figure 3 shows the environmental cell used for hydrogen testing.

Microscopic Observations

After fracture, all samples were ultrasonically cleaned in preparation for microscopic examination. Specimens were first viewed in a Bausch & Lomb 10-70x Stereoscopic Zoom Microscope (SZM) and later examined

Figure 3. Environmental Cell Used in Hydrogen Testing

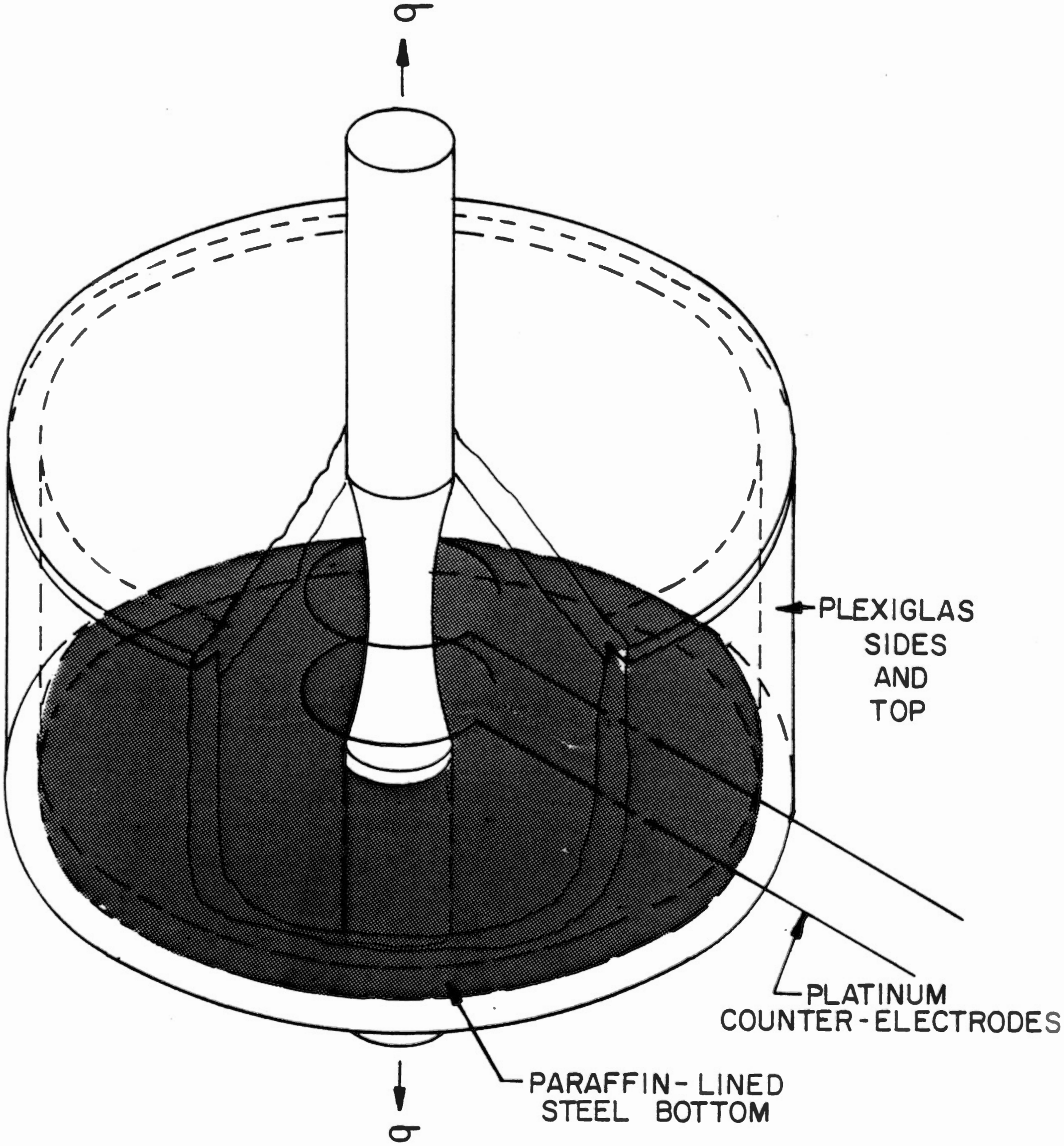
q
PLEXIGLAS SIDES AND TOP
PLATINUM COUNTER-ELECTRODES
PARAFFIN-LINED STEEL BOTTOM
q

in a Jeol Model 35 Scanning Electron Microscope (SEM). Some of the fatigue specimens were taken off the MTS prior to fracture and were examined under a Reichert optical microscope outfitted with Nomarski interference contrast equipment. This gave outstanding views of the minute height differences.

CHAPTER IV

EXPERIMENTAL RESULTS

Variation in Strain Rate

Tensile tests were performed on specimens of 250 μm average grain size. The samples were tested in air, mercury, and hydrogen. The results follow.

Tests in Air

The FCC metals like nickel and copper usually show little strain rate sensitivity [5]; consequently, little variation in mechanical properties was expected. Two tests were run in air at strain rates differing by 10^3 for comparison purposes and results are summarized in Table II. There was only a slight change in tensile strength and both samples experienced large reduction in area. Fracture surfaces were cup-and-cone (Figure 4) and no side cracking occurred. When viewed at higher magnifications in the SEM, the expected microvoids covered the surface. There was no detectable difference in void size between the two samples. Figure 5 is representative of the fractography.

Tests in Mercury

Tests were completed in mercury at five strain rates; the data are given in Table III. The pertinent features are:

TABLE II

TENSILE STRENGTH AND REDUCTION IN AREA OF MONEL 400 TESTED IN AIR

Strain Rate, s^{-1}	Tensile Strength, ksi	Reduction in Area, %
1.6×10^{-2}	94	74
1.6×10^{-5}	89	70

TABLE III

TENSILE STRENGTH AND REDUCTION IN AREA OF MONEL 400 TESTED IN MERCURY

Strain Rate, s^{-1}	Tensile Strength, ksi	Reduction in Area, %
1.6×10^{-2}	95	64
1.6×10^{-3}	93	33
1.6×10^{-4}	69	14
1.6×10^{-5}	63	11
1.6×10^{-6}	58	9

Figure 4. Fracture Surface of Monel 400 Broken in Air. The fracture surface is cup-and-cone.

Figure 5. Detail of Microvoids Covering the Fracture Surface of Monel 400 Broken in Air.

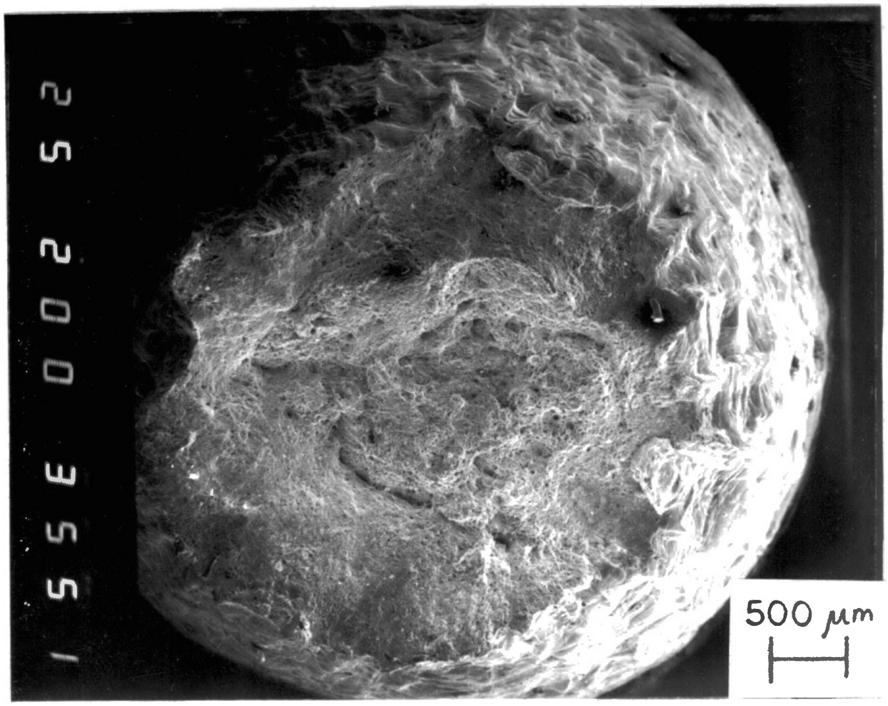
1 55E 002 52
500 µm

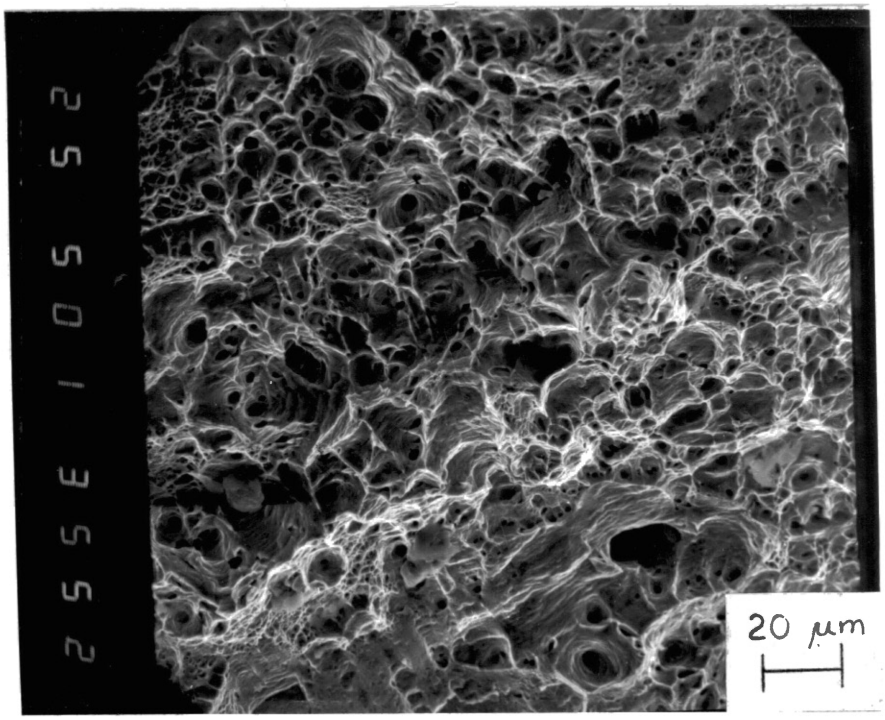
2 55E 1 05 52
20 µm

1. The alloy exhibits a large strain rate sensitivity in mercury. As strain rate decreased by a factor of 10^4, the tensile strength fell from 95 to 58 ksi.

2. Reduction in area decreased (embrittlement increased) considerably as strain rate decreased, and was accompanied by a change in fracture mode from ductile microvoids to transgranular tearing to clean intergranular cracking.

3. Side cracking was observed in all specimens except at the highest strain rate. The side cracking was largely flat (oriented 90° to the principal stress axis), with a few slant (45°) cracks linking the flat cracks. The incidence of slant cracking increased with the strain rate. By measuring the diameter of the sample at the crack farthest from the fracture, it was determined that side cracking occurred at approximately 81 ±3% of the tensile strength. The data are summarized in Table IV.

TABLE IV

EXTENT OF SIDE CRACKING IN MONEL 400 TESTED IN MERCURY

Strain Rate, s^{-1}	Farthest Crack From Fracture Surface, mm	Maximum Stress Seen by Farthest Crack, ksi	$\frac{\sigma_{max}}{TS}$, %
1.6×10^{-2}	(no side cracking)	---	---
1.6×10^{-3}	6	78	84
1.6×10^{-4}	8	54	78
1.6×10^{-5}	5	51	81
1.6×10^{-6}	10	49	84

4. Evidence of slip at the grain boundaries decreased with decreasing strain rate, as did secondary (longitudinal) cracking.

At low magnifications (~15 x) in the SEM, the fractographic features are noteworthy. At the highest strain rate in mercury, transgranular tearing seems to cover about 40 percent of the surface, while the balance is made up of microvoids (Figure 6). This contrasts with the 100 percent microvoid appearance of the sample broken in air at the same strain rate, seen earlier in Figure 4.

As the strain rate was lowered, embrittlement progressively became more severe. Figure 7 shows an overall view of a sample broken at $1.6 \times 10^{-3}\ s^{-1}$. The edges appear to have failed by transgranular tearing and much secondary (longitudinal) cracking is visible. Nearer the center of the fracture surface, relatively clean intergranular cracking predominates. Another tenfold decrease in strain rate produced somewhat cleaner intergranular cracking. Figure 8 shows a seemingly 100 percent intergranular fracture. Less secondary cracking is visible in this sample than in the previous two.

Figures 9 and 10 correspond to strain rates of $1.6 \times 10^{-5}\ s^{-1}$ and $1.6 \times 10^{-6}\ s^{-1}$, respectively. In each, individual grains appear cleanly and few secondary cracks are visible. It was felt that at a slow enough strain rate, secondary cracks would completely disappear.

Higher magnifications (~200 x) in the SEM permitted sharper contrasts to be drawn as to the extent of embrittlement. Figure 11 shows the intense plastic deformation accompanying transgranular tearing near the edge of the sample shown in Figure 6. Slip marks and secondary cracks are visible. At the next slower rate ($1.6 \times 10^{-3}\ s^{-1}$), grain boundaries are more distinct (Figure 12). This photograph was taken

Figure 6. Fracture Surface of Monel 400 Broken in Mercury at 1.6 x 10^{-2} s^{-1}. Microvoids cover over 50% of the surface, with the balance made up of transgranular tearing.

Figure 7. Fracture Surface of Monel 400 Broken in Mercury at 1.6 x 10^{-3} s^{-1}. This photograph shows tearing around the edges, and intergranular cracking near the center.

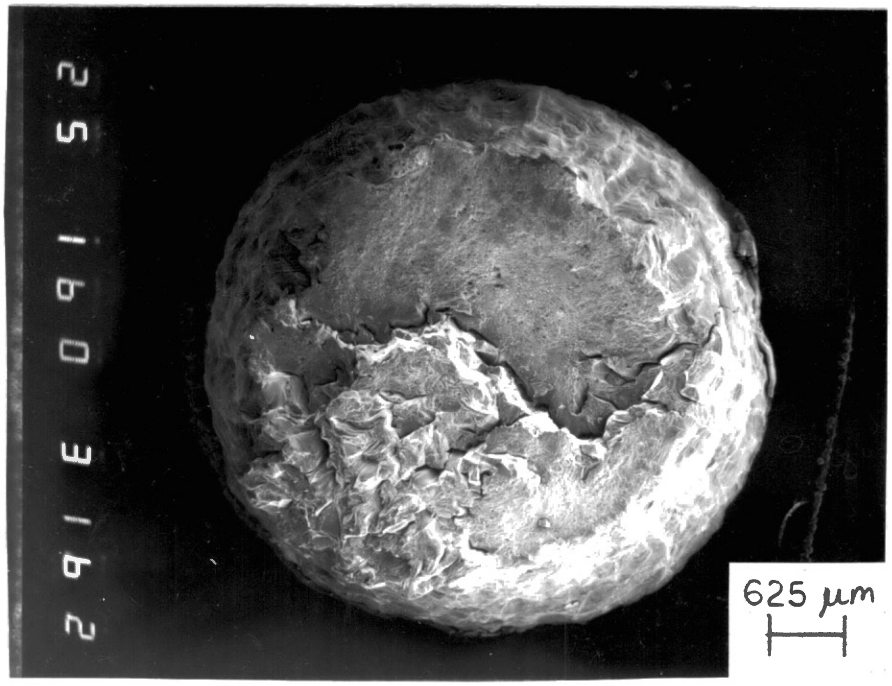
625 μm

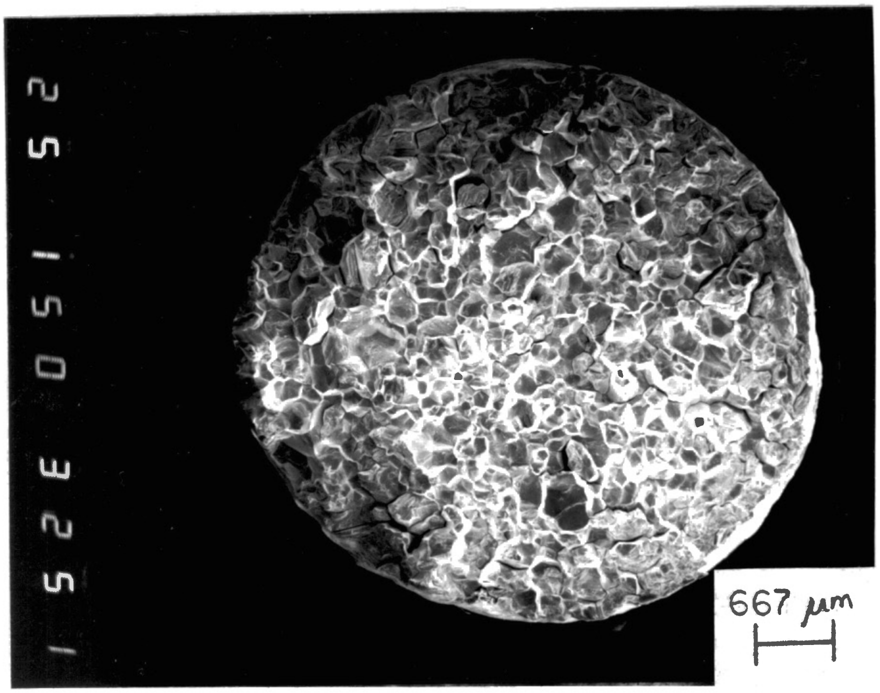
667 μm

Figure 8. Fracture Surface of Monel 400 Broken in Mercury at 1.6 x 10^{-4} s^{-1}. No tearing is visible; the entire fracture looks to be intergranular.

Figure 9. Fracture Surface of Monel 400 Broken in Mercury at 1.6 x 10^{-5} s^{-1}. Clean intergranular cracking.

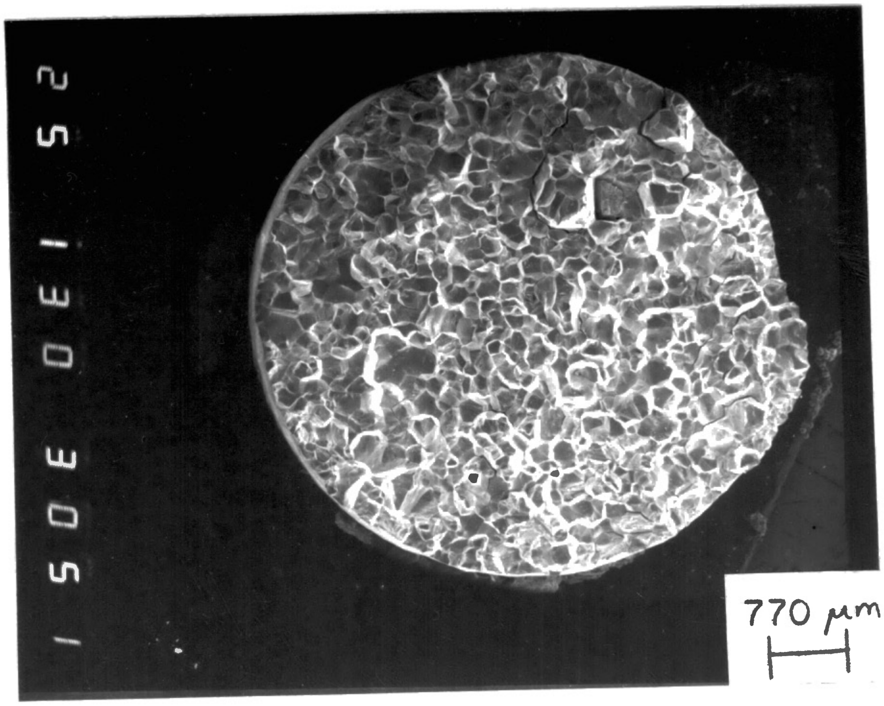
770 μm

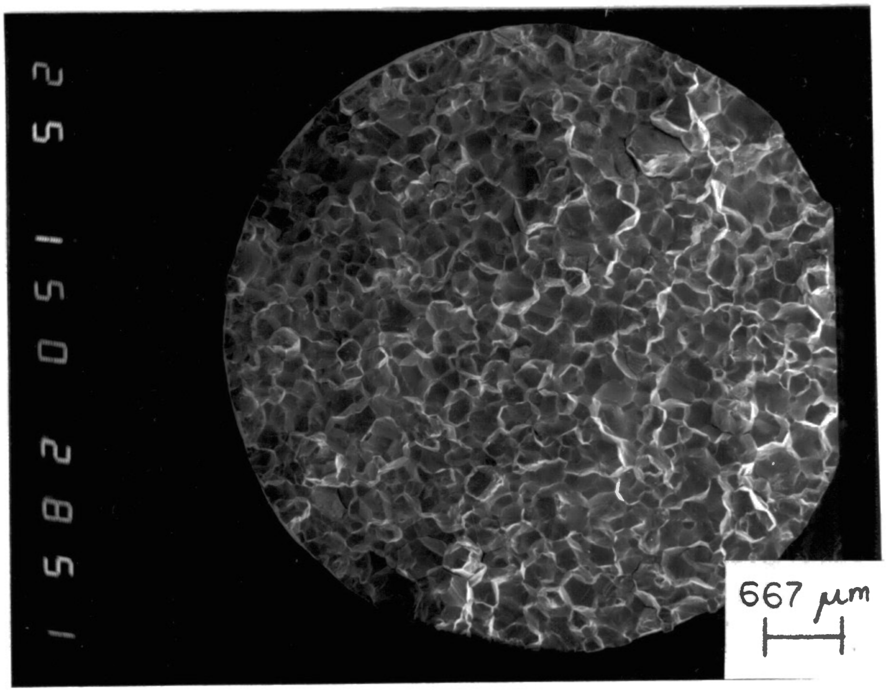
667 μm

Figure 10. Fracture Surface of Monel 400 Broken in Mercury at 1.6 x 10^{-6} s^{-1}. Clean intergranular cracking.

Figure 11. Detail of Transgranular Tearing at Lower Edge of Figure 6. Slip marks and secondary cracks are visible.

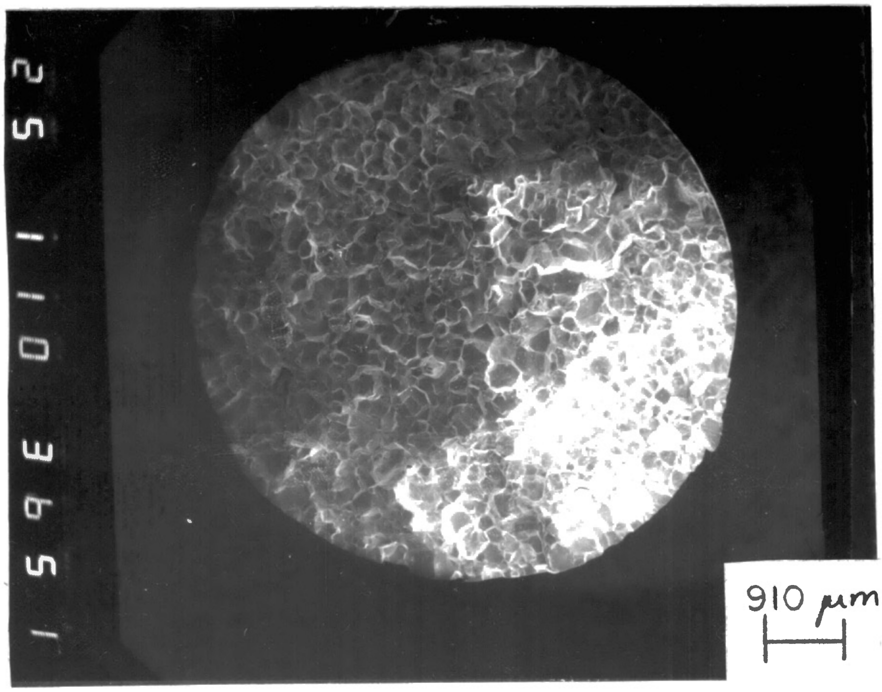
910 μm

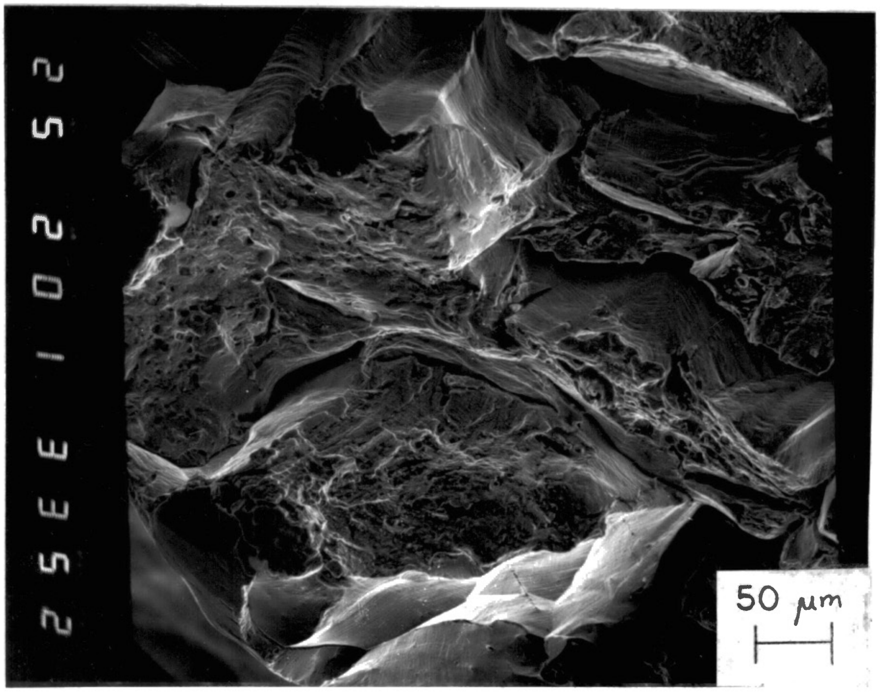
50 μm

Figure 12. Appearance of Intergranular Cracking and Light Tearing Near the Center of Figure 7. Slip marks can be seen on some grain faces, and some tearing is visible.

Figure 13. Intergranular Cracking Near the Center of Figure 8. This shows much cleaner cracking than in Figure 12, though some slip and extremely light tearing is visible.

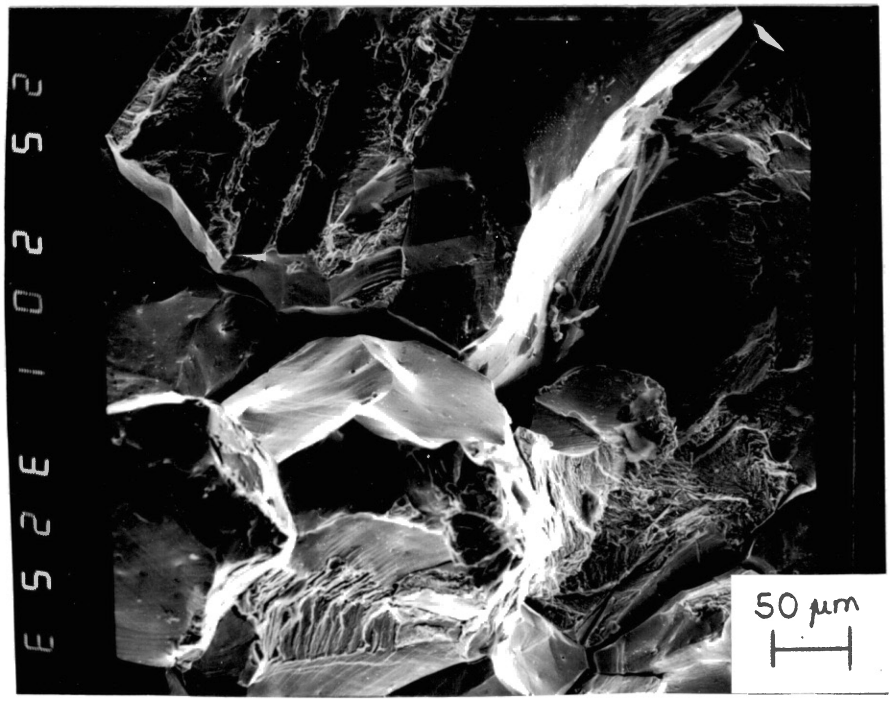
50 μm


50 μm

near the center of the sample shown in Figure 7. Slip marks are heavy on some grains, though some faces appear quite clean. The tearing and secondary cracking associated with the transgranular mode are still in evidence. In this fracture as well as the other predominantly intergranularly fractures, the incidence of tearing decreases towards the sample center. The fractography becomes noticeably cleaner (more intergranular) about three to four grains from the edge of the sample, but slip marks become slightly more apparent again at the very center.

A considerably cleaner intergranular fracture can be seen in Figure 13, corresponding to a strain rate of $1.6 \times 10^{-4}\ s^{-1}$. Some light tearing persists and faint multiple slip systems can be identified. Slip traces and tearing are nearly absent in Figure 14, taken at the center of Figure 9. The fracture is cleanly intergranular and a few scattered second-phase particles, up to 5 μm in diameter, may be seen as small pock marks. Some secondary cracking persists, though the cracks are not nearly as gaping as those in the higher strain rate samples.

At the very slowest strain rate, the fracture is utterly clean intergranular near the center (Figure 15). The grain surfaces show the same pock marks as in Figure 14, but are conspicuously free from slip marks, tearing, and secondary cracking.

These tests brought up an interesting question: Was the variation in degree of embrittlement already documented strictly a function of strain rate, or was an incubation period involved in the embrittlement process? That is to say, would a sample loaded quickly to a high stress level in mercury, and then held, eventually fail under the static load? In an attempt to answer these questions, chemically polished samples were tested at two static loads. These samples were held at load for a

Figure 14. Clean Intergranular Cracking at the Center of Figure 9. A few scattered second phase particles and faint slip traces may be seen.

Figure 15. Utterly Clean Intergranular Cracking at the Center of Figure 10. Some second phase particles are present, but slip and tearing are not seen.

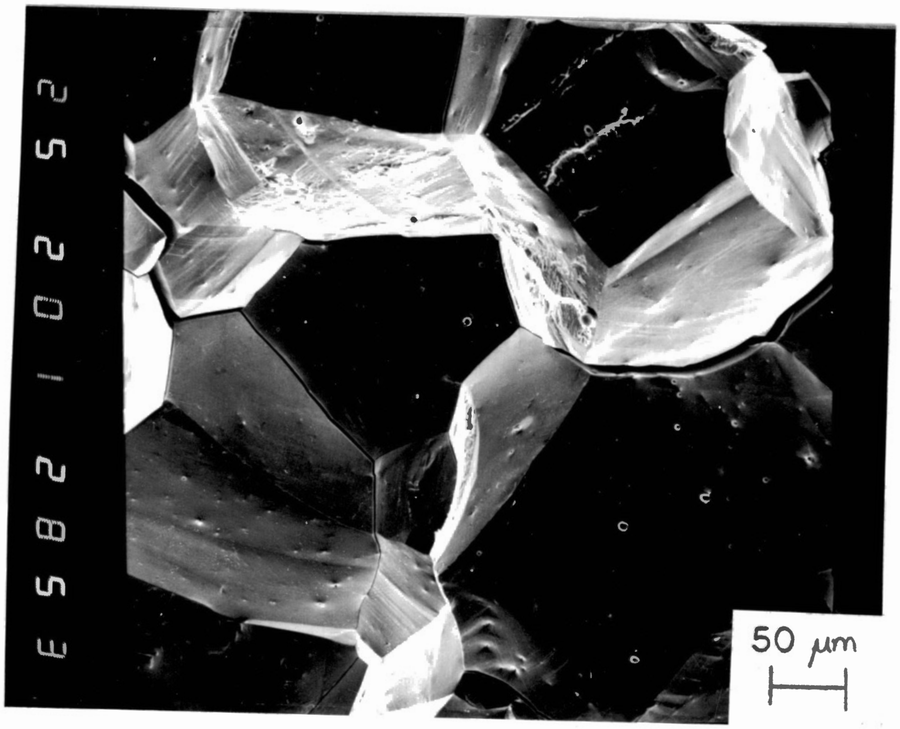
25 201 2853
50 µm

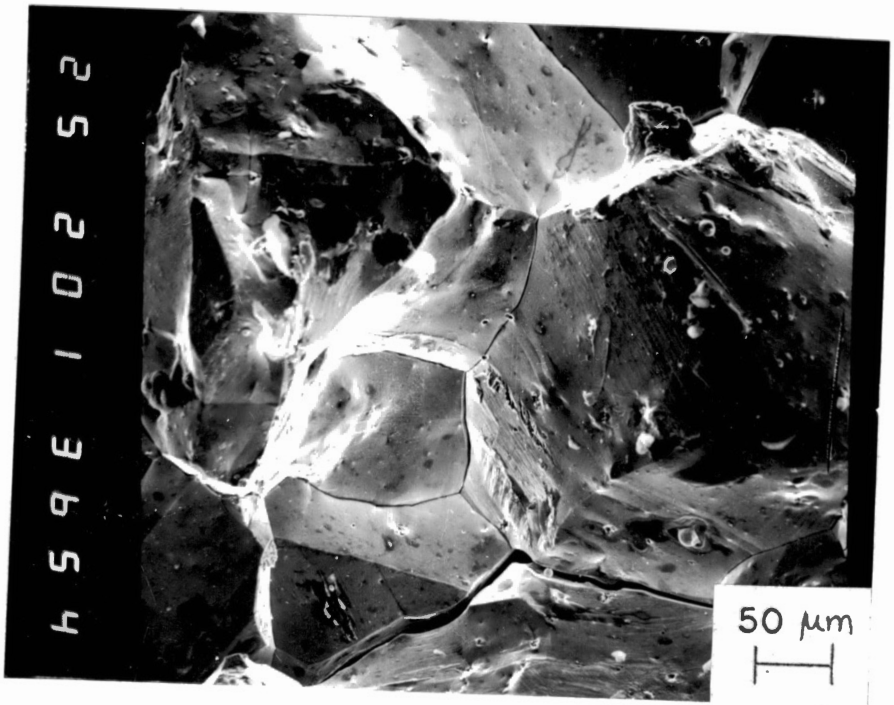
25 201 3654
50 µm

time considerably longer than the usual length of the standard dynamic tensile tests; still, no failures occurred. The 50 ksi test was interrupted at 6, 25, 93, 11, and 133 hours and the surface was examined under the SZM for evidence of the beginnings of cracks. No cracks were found; however, slip marks were visible on individual grains and an intense band of plastic deformation circled the center of the sample. This band of deformation did not enlarge or change substantially after it was first noted at the 25 hour mark. After being held at a high static load, the samples were fractured in slow strain rate tensile tests. Results are presented in Table V.

TABLE V

RESULTS OF STATIC/TENSILE TESTS
OF MONEL 400 IN MERCURY

Static Load, ksi	Time at Load, hrs	Strain Rate During Tensile Test, s^{-1}	Tensile Strength, ksi	Reduction in Area, %
63	20	1.6×10^{-5}	76	16
50	150	1.6×10^{-6}	69	15

When compared with the standard tensile test data shown in Table III, some results are surprising. The samples held at a static load and then dynamically broken showed approximately 20 percent higher tensile strengths and over 50 percent more reduction in area than the samples broken in the standard tensile test at a corresponding strain rate.

Tests in Hydrogen

Tests were run at three strain rates in hydrogen; the data are shown in Table VI. Higher strain rates were not used because of charging rate limitations which would raise the question of whether hydrogen access to the advancing crack would become a limiting factor. The features of interest include:

1. Hydrogen is a less potent embrittler than mercury in Monel 400. Strain rates which gave 100 percent intergranular cracking in mercury caused predominantly transgranular tearing in the presence of hydrogen. The tensile strengths of samples tested in hydrogen were between the tensile strengths of the samples tested in air and mercury.

2. Consistent with the tests in mercury, embrittlement increased considerably with decreasing strain rate. A 100 percent intergranular fracture was never observed in the hydrogen tests; on the contrary, an upper limit to the extent of embrittlement seemed to occur.

3. Side cracking was extensive in the samples fractured in the presence of hydrogen, but side cracking occurred at a higher proportion of the tensile strength than in the mercury tests (95% for hydrogen vs. 81% for mercury), as shown in Table VII. As in mercury, the flat cracks dominated but some slant cracks were observed, and their proportion increased with strain rate.

Variations in fractography were less obvious in the hydrogen samples viewed at low magnifications in the SEM. Figure 16 shows an overall view of the sample tested at a strain rate of $1.6 \times 10^{-4}\ s^{-1}$. The interior is mostly microvoids, and only the edges show tearing and a little cracking. At a tenfold lower strain rate, a much larger area

TABLE VI

TENSILE STRENGTH AND REDUCTION IN AREA OF MONEL 400 TESTED IN HYDROGEN

Strain Rate, s^{-1}	Tensile Strength, ksi	Reduction in Area, %
1.6×10^{-4}	91	56
1.6×10^{-5}	83	32
1.6×10^{-6}	82	30

TABLE VII

EXTENT OF SIDE CRACKING IN MONEL 400 TESTED IN HYDROGEN

Strain Rate, s^{-1}	Farthest Crack From Fracture Surface, mm	Maximum Stress Seen by Farthest Crack, ksi	$\frac{\sigma_{max}}{TS}$, %
1.6×10^{-4}	10	88	97
1.6×10^{-5}	9	77	92
1.6×10^{-6}	8	79	96

Figure 16. Fracture Surface of Monel 400 Broken in Hydrogen at 1.6×10^{-4} s^{-1}. Microvoids dominate; some tearing can be seen on the periphery.

Figure 17. Fracture Surface of Monel 400 Broken in Hydrogen at 1.6×10^{-5} s^{-1}. Tearing is much more extensive than in Figure 16. Some individual grains may be seen near the edge.

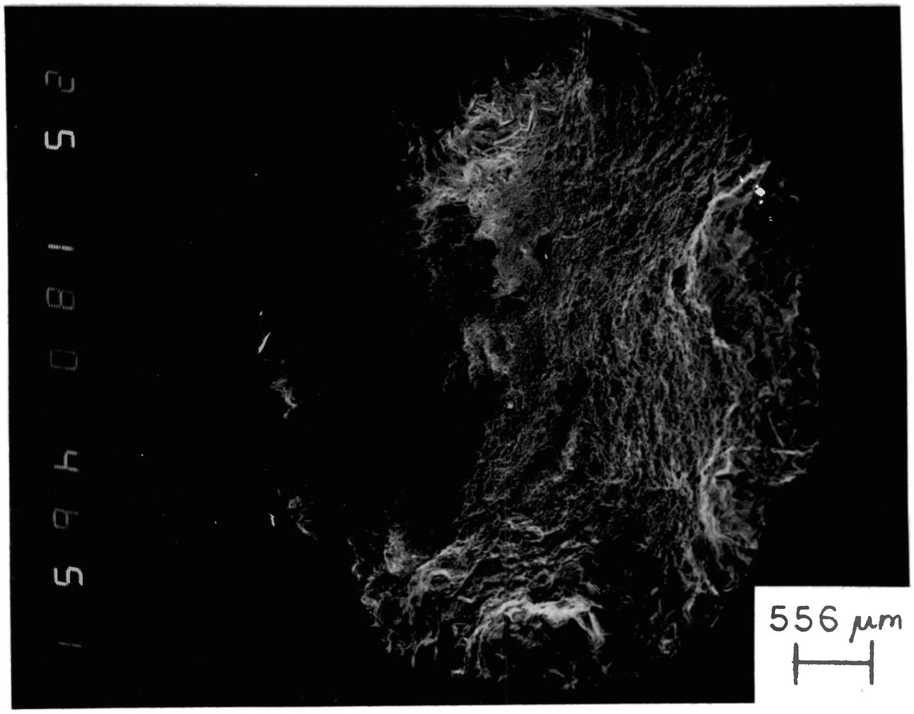
556 µm

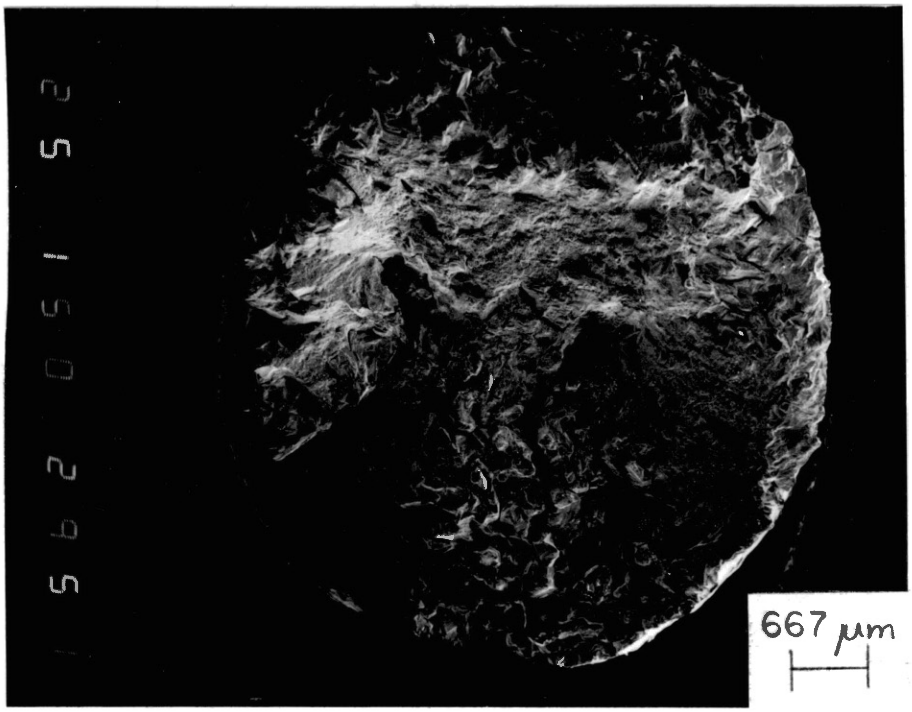
667 µm

experienced embrittlement, as shown in Figure 17. Some grain faces can be seen and many gaping secondary cracks are visible. Little difference in the fractography was apparent when the strain rate was lowered another factor of 10 (Figure 18). Approximately the same proportion of the fracture surface is covered by voids and the tearing/cracking features also appear to be quite similar. The inference is that some sort of limit was reached as to the extent of embrittlement and another order of magnitude decrease in strain rate would give substantially the same results. This theory could not be confirmed though, due to limitations in the test equipment.

Higher magnifications in the SEM confirmed the earlier observations. Figure 19, taken at the edge of the sample shown in Figure 16, shows the entire transition from clean intergranular facets to transgranular tearing and secondary cracking to void coalescence, in a distance of about 1 mm. Figure 20, taken at the edge of the sample shown in Figure 17 shows mixed intergranular cracking and transgranular tearing. Slip marks are visible on most of the grain faces and many secondary cracks are present. The fractography is almost indistinguishable from that shown in Figure 21, photographed at the edge of the sample shown in Figure 18. The difference, however, is that the latter was taken on a sample tested at a ten times slower rate than the former. Nearer the center of both samples, the fractography remained strikingly similar. Figures 22 and 23 were taken in the interiors of Figures 17 and 18, respectively. Both show gaping secondary cracks, intense tearing, and the beginnings of a transition to microvoids. These similarities throughout the samples reinforce the inference of an embrittlement limit for the stated grain size and hydrogen charging rate.

Figure 18. Fracture Surface of Monel 400 Broken in Hydrogen at 1.6 x 10^{-6} s^{-1}. Little change is seen from appearance of Figure 17.

Figure 19. Rapid Transition of Fracture Mode at the Edge of Figure 16. At lower left, a few clean intergranular faces mix with transgranular tearing. Microvoids dominate at upper right, nearer the center of the sample.

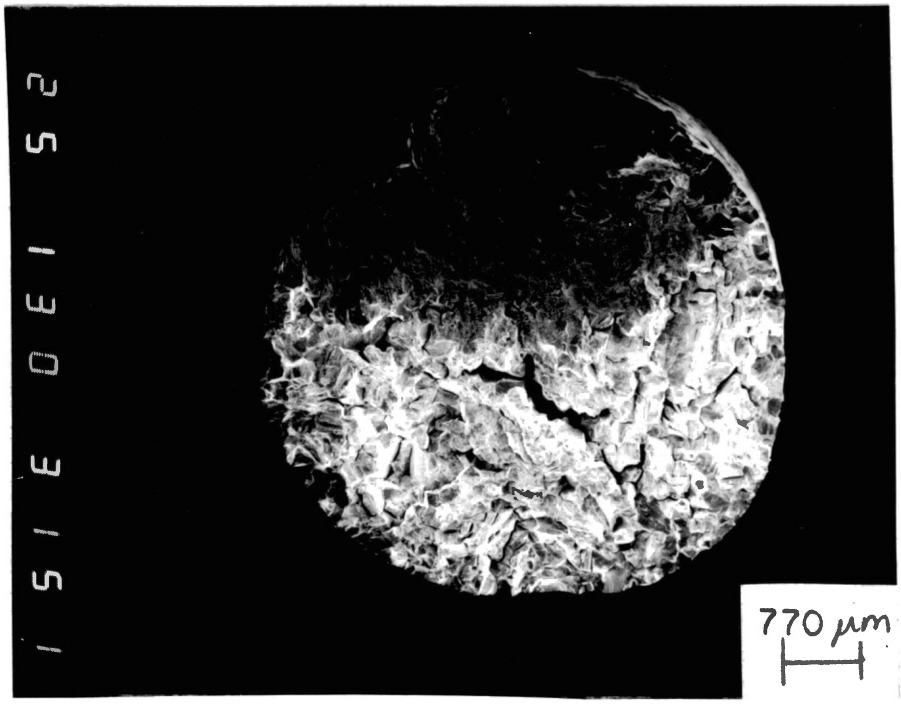
770 µm

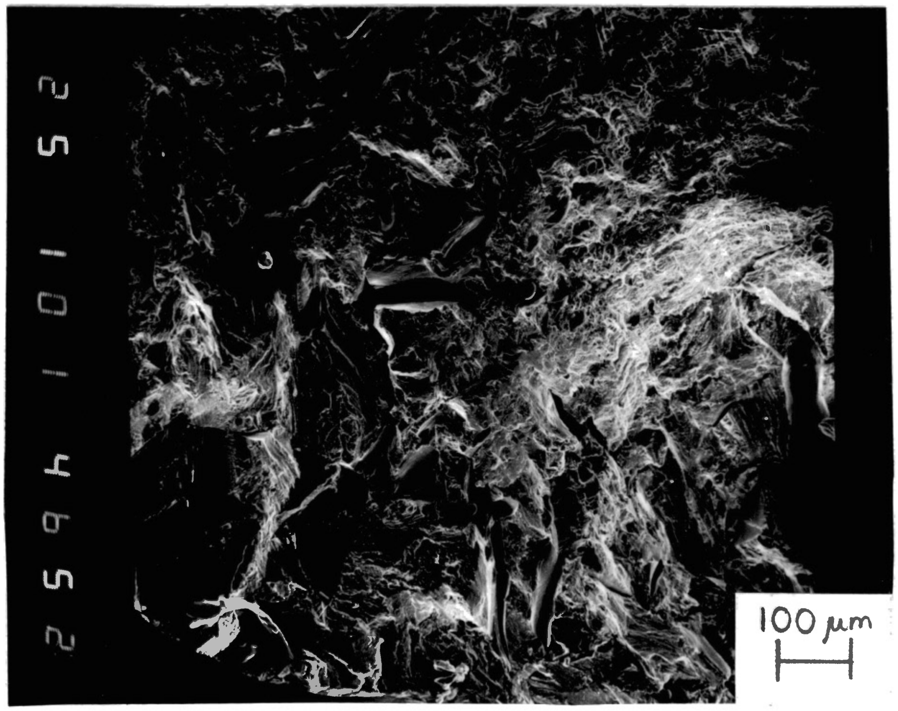
100 µm

Figure 20. Mixed Intergranular and Transgranular Zone at the Edge of Figure 17. The strain rate was 1.6×10^{-5} s^{-1}.

Figure 21. Mixed Intergranular and Transgranular Zone at the Edge of Figure 18. Note the similarity to Figure 20, where the strain rate was ten times faster.

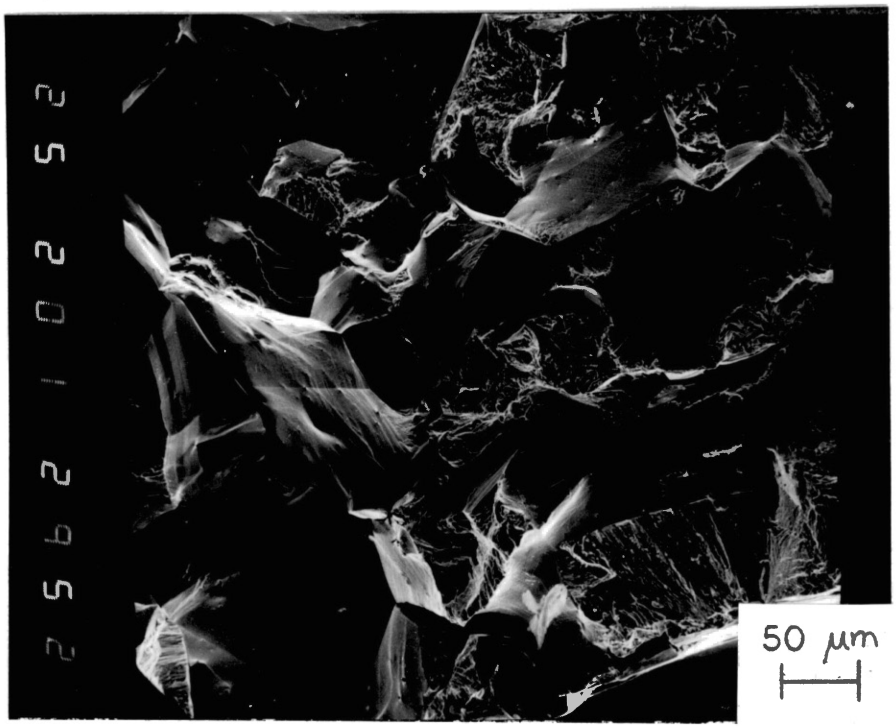
50 μm

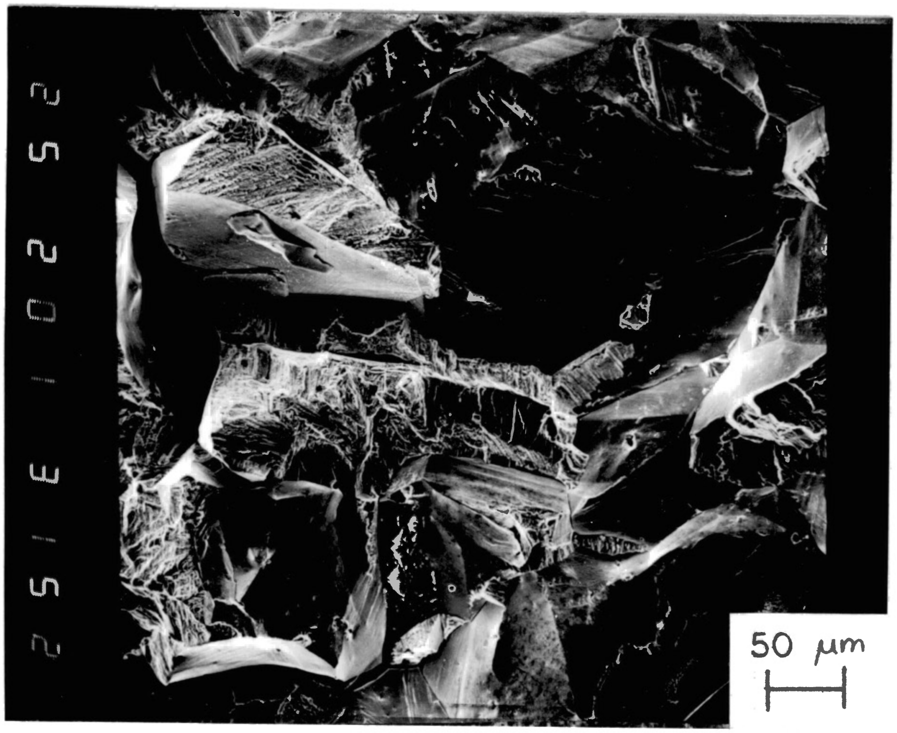
50 μm

Figure 22. Tearing, Cracks, and Microvoids at the Center of Figure 17.

Figure 23. Tearing and Cracks Near the Center of Figure 18. The appearance is virtually the same as Figure 22.

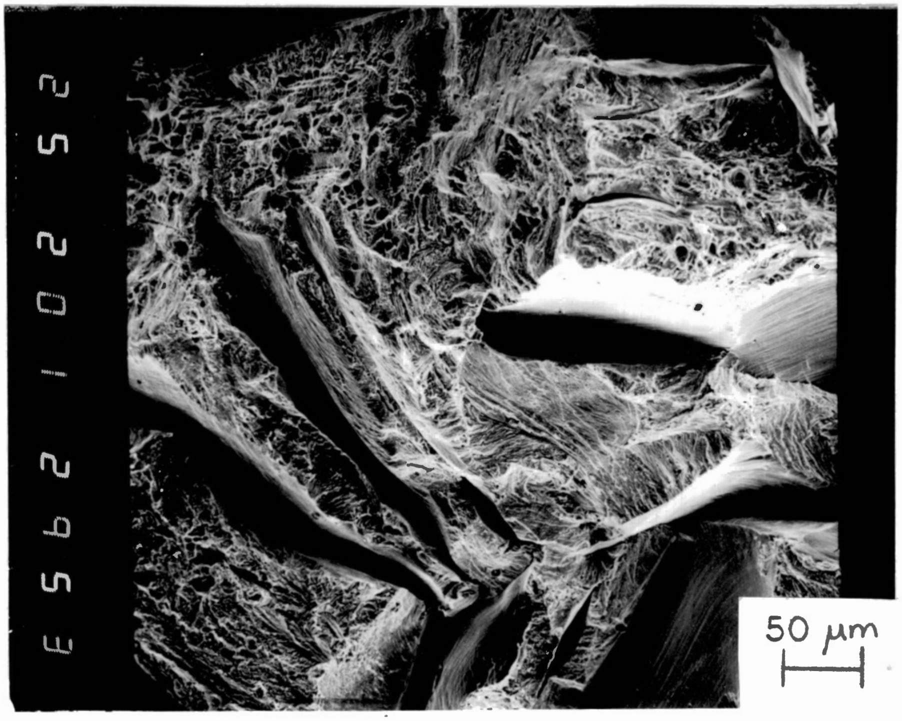
50 μm

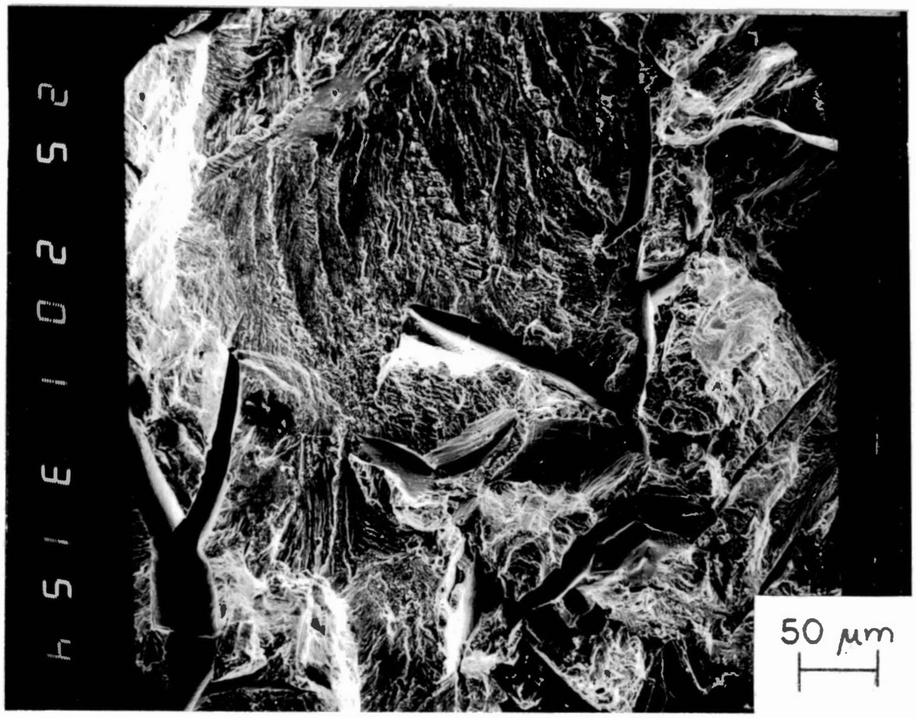
50 μm

A question raised by these tests was whether the transition in fracture appearance with depth of penetration was due to limited hydrogen penetration, and whether different diameters would give different tensile strengths. This question was explored for three different diameters (Table VIII). There was a very small increase in tensile strength with increasing diameter, but the depth of the intergranular/transgranular zone remained approximately constant. It was not clear whether the transition near the center was due to a critical stress intensity or lack of available hydrogen.

TABLE VIII

EFFECT OF SAMPLE DIAMETER ON MONEL 400
TESTED IN HYDROGEN

Sample Diameter, mm	Tensile Strength, ksi	Reduction in Area, %	Depth of Appearance of Microvoids, mm
3.63	80	20	2.0
6.35	83	32	3.0
9.78	84	37	2.5

Variation in Grain Size

Tensile tests were performed in air, mercury, and hydrogen at room temperature for a variety of grain diameters ranging from 35 to 500 μm. The strain rate was held at a constant $1.6 \times 10^{-5}\ s^{-1}$ for these tests and the results appear below.

Tests in Air

Two grain sizes were tested in air: fine-grained (35 μm) and coarse-grained (250 μm). The results are presented in Table IX. As expected, the grain size had only a minor effect on the tensile strength and ductility of the samples. The fractures were cup-and-cone; failure was by microvoid coalescence.

TABLE IX

VARIATION OF TENSILE STRENGTH AND REDUCTION IN AREA WITH GRAIN SIZE OF MONEL 400 TESTED IN AIR

Grain Diameter, μm	Hardness, R_B	Tensile Strength, ksi	Reduction in Area, %
35	70	92	67
250	57	89	70

Tests in Mercury

Five different grain sizes were tested in mercury. The data are given in Table X. Interesting points are:

1. The tests showed a conspicuous decrease in tensile strength in the presence of mercury. Embrittlement, when measured as the decrease in tensile strength and reduction in area, tended to increase with increasing grain size. An exception was the ultra-coarse (500 μm) sample, which exhibited relatively high strength and good ductility.

TABLE X

VARIATION OF TENSILE STRENGTH AND REDUCTION IN AREA WITH GRAIN SIZE OF MONEL 400 TESTED IN MERCURY

Grain Diameter, μm	Hardness, R_B	Tensile Strength, ksi	Reduction in Area, %
35	70	73 92 air	12
80	64	71	11
150	59	63	12
250	57	63 89 air	11
500	54	84	31

TABLE XI

VARIATION OF THE EXTENT OF SIDE CRACKING WITH GRAIN SIZE OF MONEL 400 TESTED IN MERCURY

Grain Diameter, μm	Farthest Crack From Fracture Surface, mm	Maximum Stress Seen by Farthest Crack, ksi	$\frac{\sigma_{max}}{TS}$, %
35	1	73	100
80	4	75	98
150	5	54	86
250	5	51	81
500	10	60	71

2. Fractures were generally intergranular with some transgranular tearing near the sample edge. No obvious transition occurred in the fracture mode as grain size varied, except for the 500 μm grain size.

3. Side cracking was more extensive in the larger-grained samples. Also, the relative stress level at which side cracking occurred decreased with increasing grain size, as shown in Table XI (page 51). The coarser-grained (hence softer) samples experienced more plastic deformation at a given stress. This caused greater accommodation between individual grains and more side cracking.

Electron microscopy revealed little difference between the samples other than the large variations in grain size. Figures 24 through 27 show seemingly 100 percent intergranular fractures in the range of grain sizes from 35 to 250 μm. In the 500 μm sample, however, a change in fracture mode has taken place (Figure 28). A mixture of intergranular and transgranular features is visible even at low magnifications. Secondary cracks are also quite clear.

Higher magnifications (200 x to 500 x) fail to show significant fractographic differences in the four finest-grained samples. The 80 μm grain size is typical: at the edge, tearing, secondary cracking, and intergranular cracking are observed (Figure 29), while nearer the center, the fracture seen in Figure 30 is quite clean intergranular cracking.

A sharp contrast is seen in the coarsest grain size. Figure 31 shows mostly transgranular tearing and secondary cracking, with a few intergranular facets visible.

Tests in Hydrogen

As in mercury, tests were run for five different grain sizes; the

Figure 24. Fracture Surface of 35 μm Grain Size Monel 400 Broken in Mercury. The fracture appears to be 100% intergranular.

Figure 25. Fracture Surface of 80 μm Grain Size Monel 400 Broken in Mercury

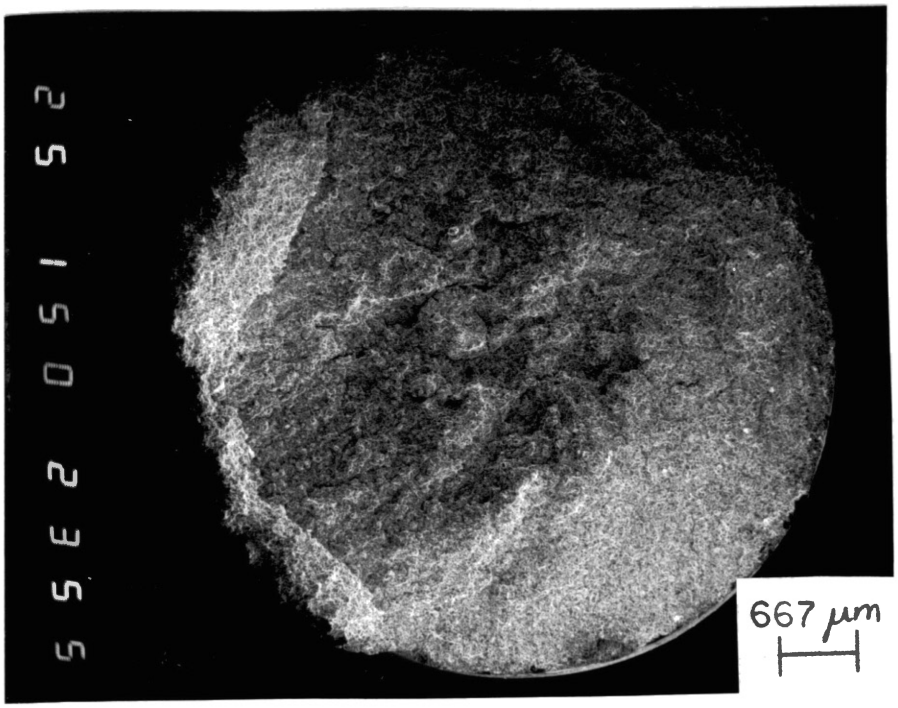
667 μm

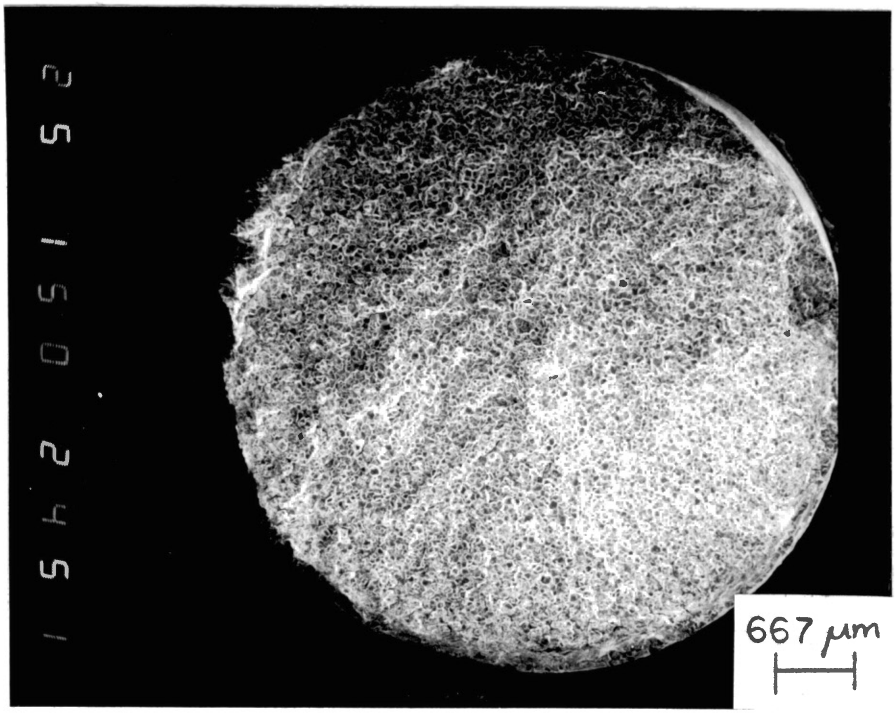
667 μm

Figure 26. Fracture Surface of 150 μm Grain Size Monel 400 Broken in Mercury

Figure 27. Fracture Surface of 250 μm Grain Size Monel 400 Broken in Mercury

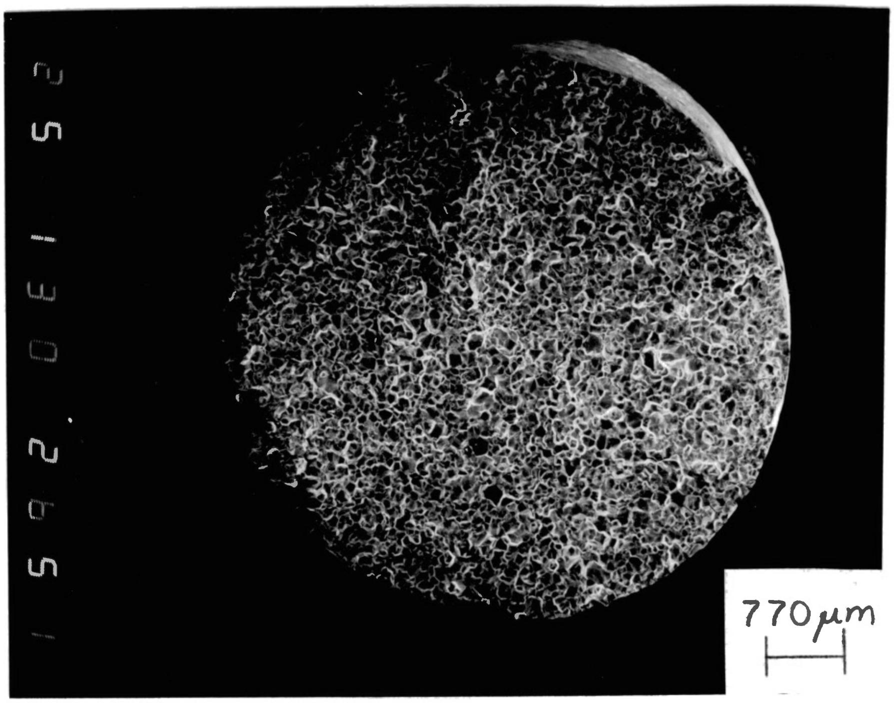
770 μm

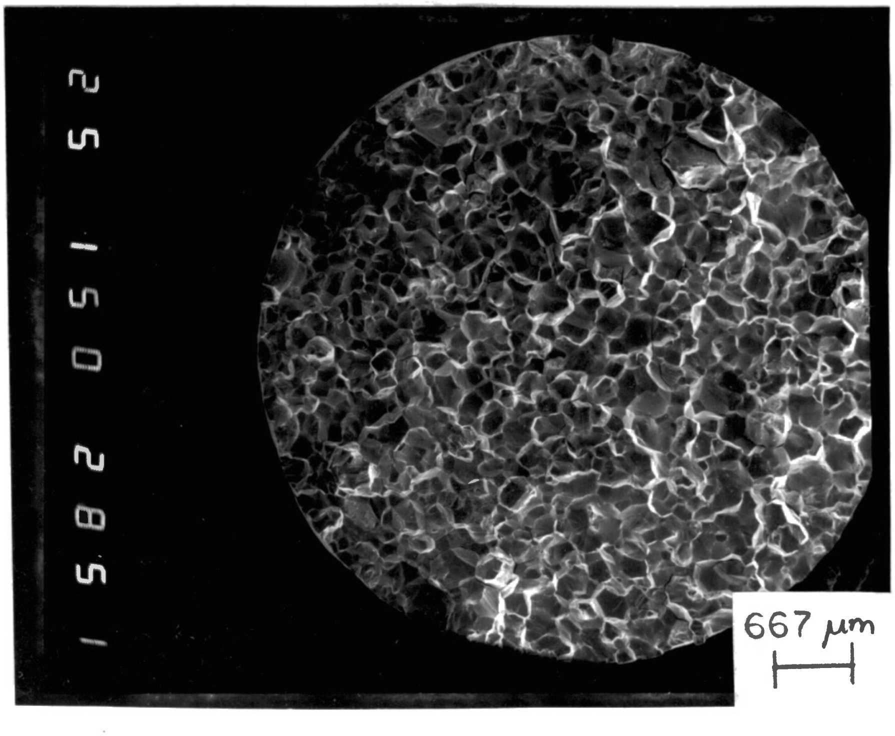
667 μm

Figure 28. Fracture Surface of 500 μm Grain Size Monel 400 Broken in Mercury. In contrast to Figures 24-27, the surface is a mix of intergranular and transgranular, with huge secondary cracks.

Figure 29. Intergranular Cracking Mixed With Tearing at the Edge of Figure 25. This was typical of the four finest-grained samples broken in mercury.

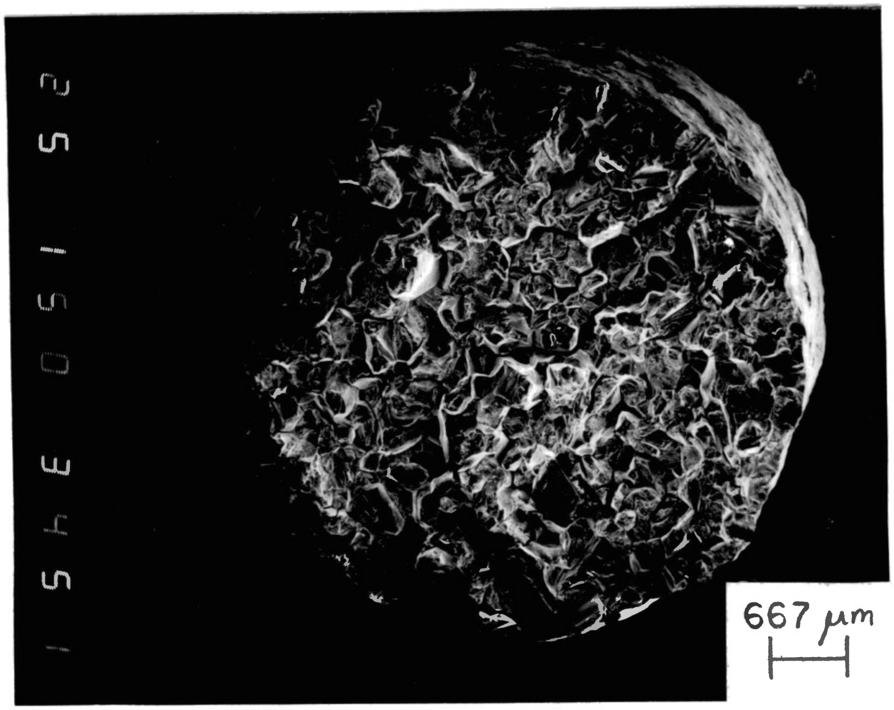
667 μm

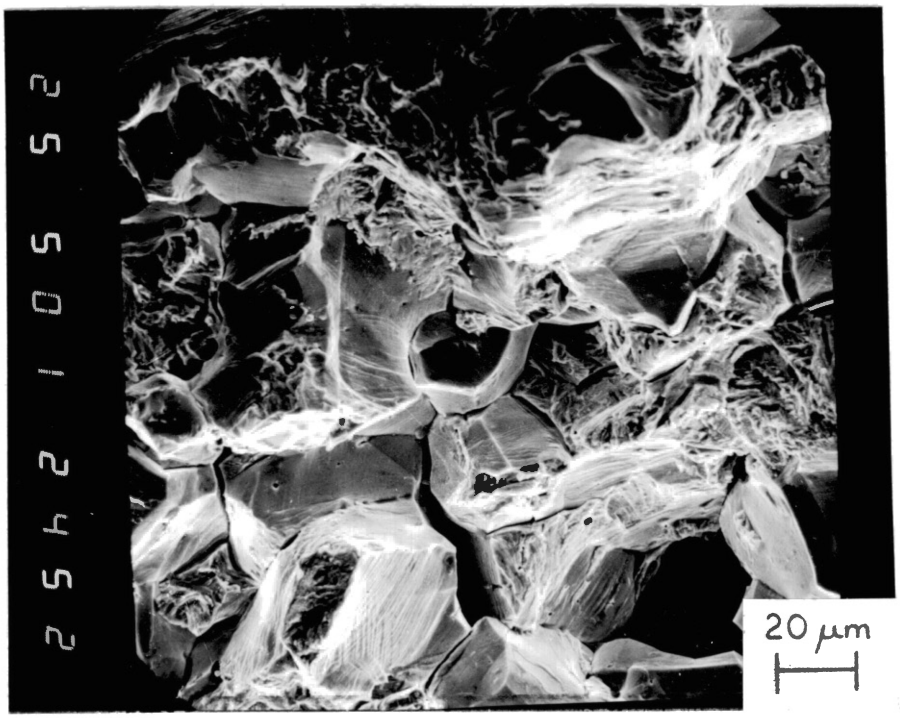
20 μm

Figure 30. Intergranular Cracking in the Interior of Figure 25. Again, this was representative of the four finest-grained samples.

Figure 31. Transgranular Tearing at the Center of Figure 28. This contrasts with the utterly brittle fracture seen in Figure 30.

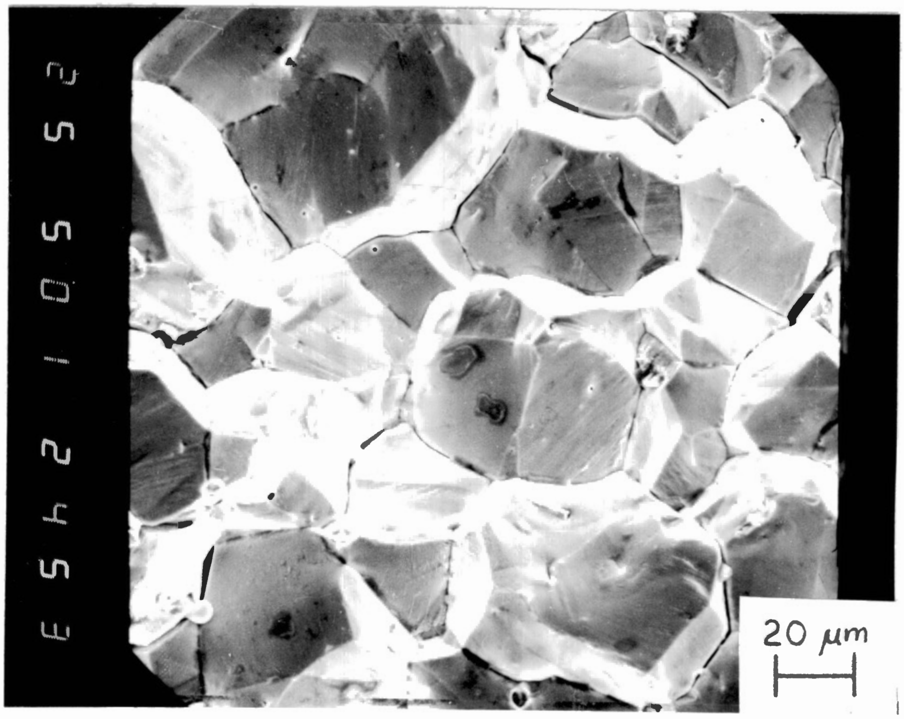
20 µm

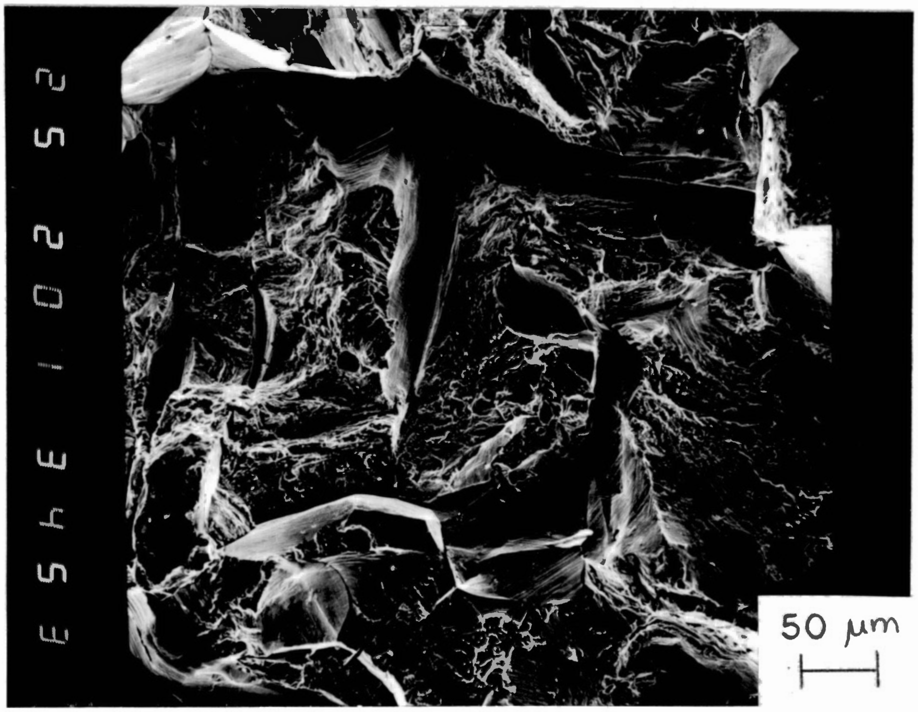
50 µm

data are summarized in Table XII. Key points include the following:

1. A small decrease in tensile strength was noted for the specimens tested in hydrogen, but the loss of strength was less in hydrogen than in mercury.

2. The reduction in area is much less in hydrogen than in air. Reduction in area generally increased with increasing grain size; i.e., the embrittlement generally decreased.

3. Side cracking was heavier in the larger grain sizes. As in mercury, the relative stress at which cracking occurred was lower in the larger-grained samples. The data can be seen in Table XIII.

The lower magnification photographs from the SEM reflect closely the trend of decreasing embrittlement with increasing grain size. Figure 32 shows the finest-grained sample at a 20° tilt for clarity. The exterior two-thirds of the sample is covered by a mix of intergranular cracking and transgranular tearing, while the center is microvoids. A slightly larger proportion of voids is seen in Figure 33. The voids constitute the lightest-colored band and run generally southwest to northeast. Regions of cracking and tearing are also visible.

Microvoids cover over half the surface of the 150 μm grain sample (Figure 34). Three distinct areas of tearing and secondary cracking are seen at the edges and little or no intergranular cracking is apparent. The 250 μm test appears not to fit the pattern of decreasing embrittlement, in terms of both reduction in area and fractography. This sample was shown earlier in Figure 17. A few clean intergranular faces can be seen at the lower edge, but the fracture is largely transgranular with heavy secondary cracking. Voids cover about 30 percent of the surface. Figure 35 shows a large void area covering well over half of the coarsest-

TABLE XII

VARIATION OF TENSILE STRENGTH AND REDUCTION IN AREA WITH GRAIN SIZE OF MONEL 400 TESTED IN HYDROGEN

Grain Diameter, µm	Hardness, R_B	Tensile Strength, ksi	Reduction in Area, %
35	70	80 92.07	12
80	64	81	19
150	59	86	43
250	57	83 [illegible]	32
500	54	85	45

TABLE XIII

VARIATION OF THE EXTENT OF SIDE CRACKING WITH GRAIN SIZE OF MONEL 400 TESTED IN HYDROGEN

Grain Diameter, µm	Farthest Crack From Fracture Surface, mm	Maximum Stress Seen by Farthest Crack, ksi	$\frac{\sigma_{max}}{TS}$, %
35	1	81	100
80	8	81	100
150	10	82	96
250	10	76	92
500	12	71	84

Figure 32. Fracture Surface of 35 µm Grain Size Monel 400 Broken in Hydrogen. The outer ring is a mix of intergranular and transgranular, while the center is covered with microvoids.

Figure 33. Fracture Surface of 80 µm Grain Size Monel 400 Broken in Hydrogen. Voids cover a slightly larger region than in Figure 32, and run from lower left to upper right.

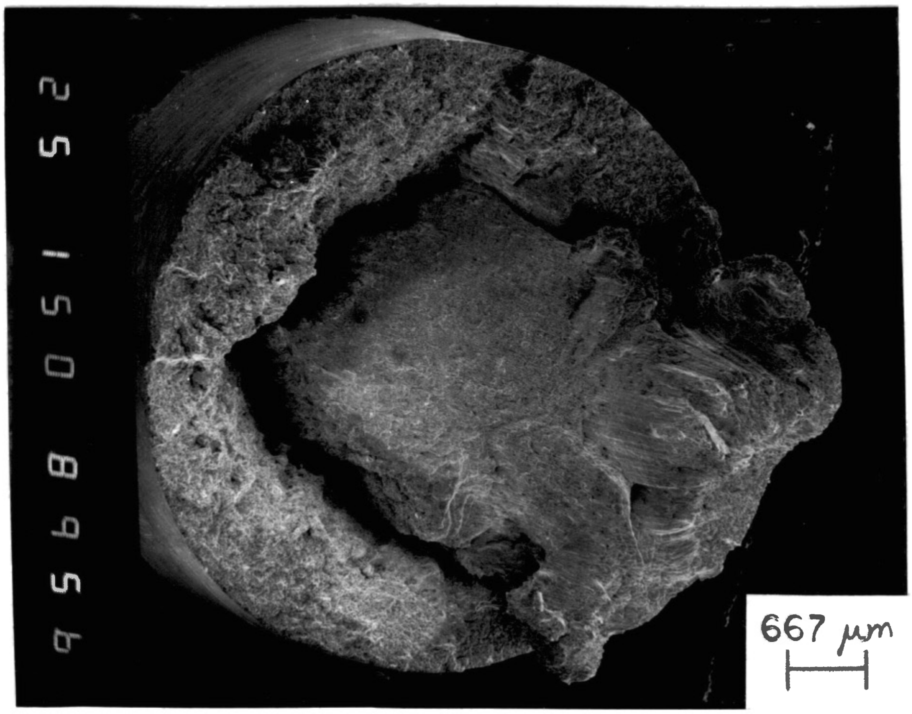
667 µm

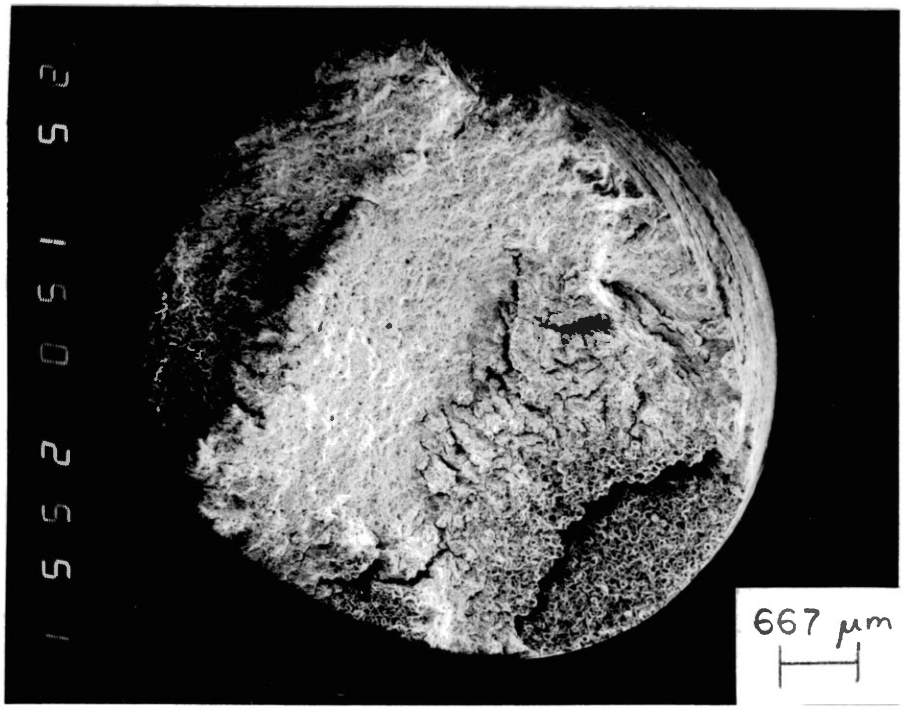
667 µm

Figure 34. Fracture Surface of 150 μm Grain Size Monel 400 Broken in Hydrogen. Voids cover over half the surface in this photograph, while tearing and secondary cracking may be seen around the edges.

Figure 35. Fracture Surface of 500 μm Grain Size Monel 400 Broken in Hydrogen. In this photograph, the coarsest-grained sample, microvoids cover well over half of the fracture surface.

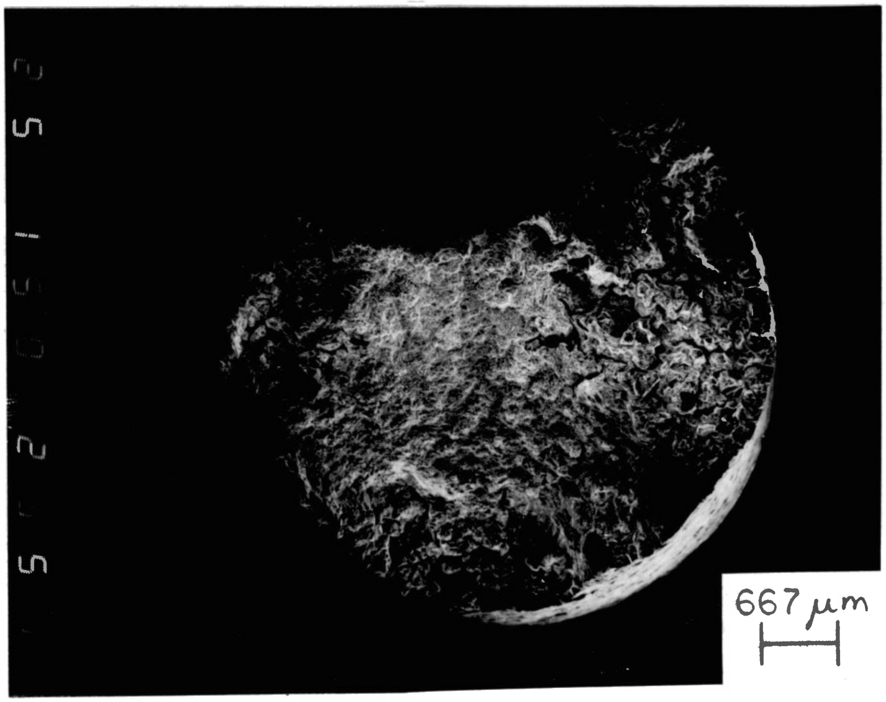
667 μm

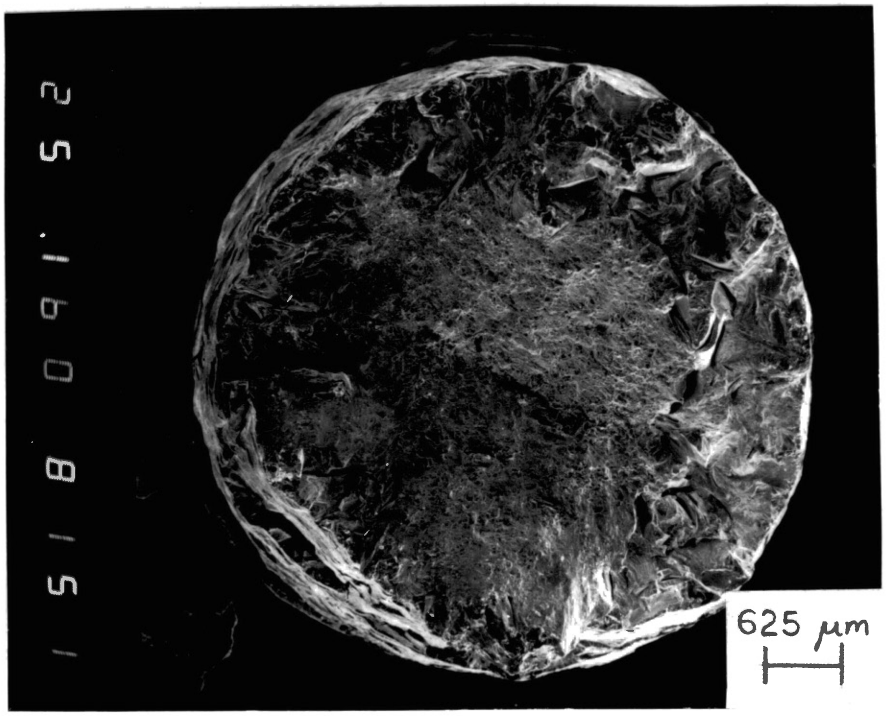
625 μm

grained samples cracking and possibly tearing can be seen around the edges.

Comparisons made at higher magnification show that the most embrittled areas of each sample (near the edges) reflect the general trend already presented. Figure 36 shows mostly intergranular cracking and some tearing at the edge of the finest-grained sample. Figure 37, taken near the edge of the 80 μm grain size sample, shows relatively clean intergranular cracking also. The major difference in these two samples (besides grain size) was that the intergranular area was larger in the finest-grained sample.

In the coarser-grained samples, a quick transition away from the intergranular mode can be seen. Figure 38 shows the rapid onset of tearing and secondary cracking quite near the edge of the 150 μm grain-size sample. In Figure 20, seen previously, the intergranular holds the general pattern toward decreasing embrittlement in the coarser-grained sizes. Figure 39 shows the transition from intergranular to transgranular less than one grain in from the surface in the 500 μm grain size. This sample showed complete transition to microvoids at two grains in from the edge.

Fatigue Tests

Fatigue tests run on Monel 400 and other nickel alloys by Price and Good [8] in mercury have shown sharply reduced lives, while tests run in hydrogen by Traylor [9] showed somewhat lower lives than tests run in air. These tests were done on fine-grained annealed specimens at a stress level of 60 ksi. The data for Monel 400 are presented in Table XIV.

Figure 36. Intergranular Cracking Covering the Edge of Figure 32. Some tearing and secondary cracking is visible.

Compare LJT p153

Figure 37. Relatively Clean Intergranular Cracking Near the Edge of Figure 33. The area of intergranular cracking in this sample was smaller than in the 80 μm sample.

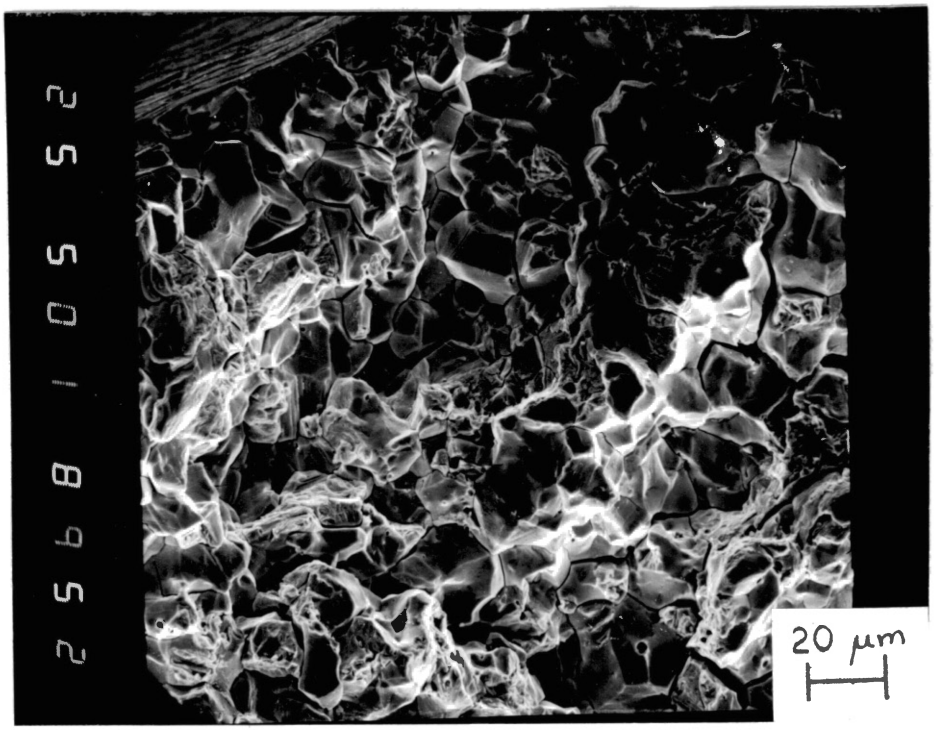
20 μm

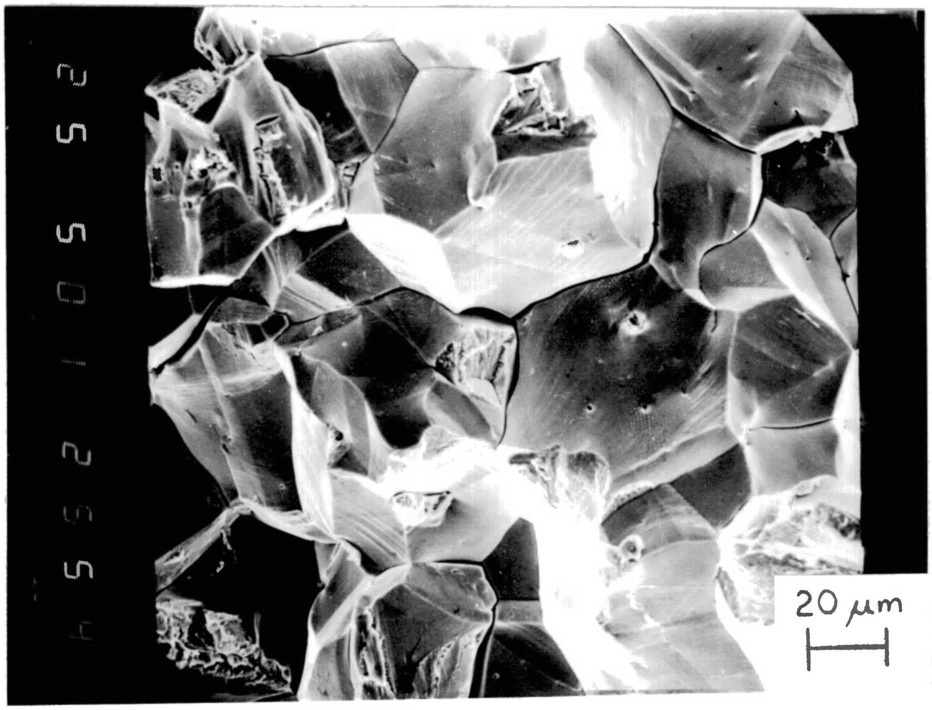
20 μm

Figure 38. Tearing and Cracking Near the Edge of Figure 34. Moving upward away from the sample edge, the transition from intergranular to transgranular is quite rapid.

Figure 39. Intergranular-to-Transgranular Transition at the Edge of Figure 35. This sample showed complete transition to microvoids just two grains (~1 mm) in from the edge.

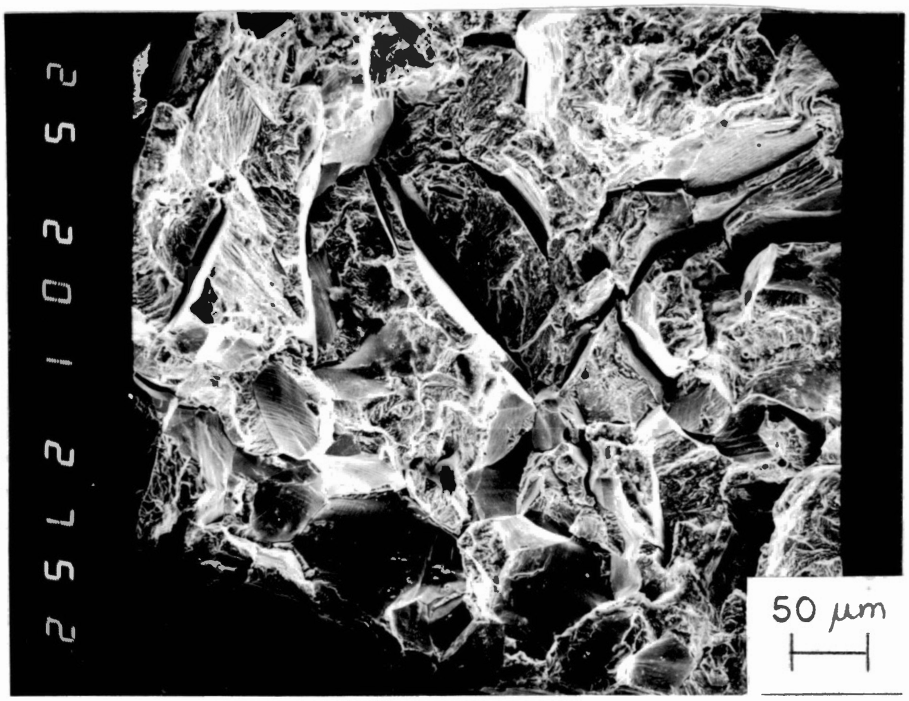
50 µm

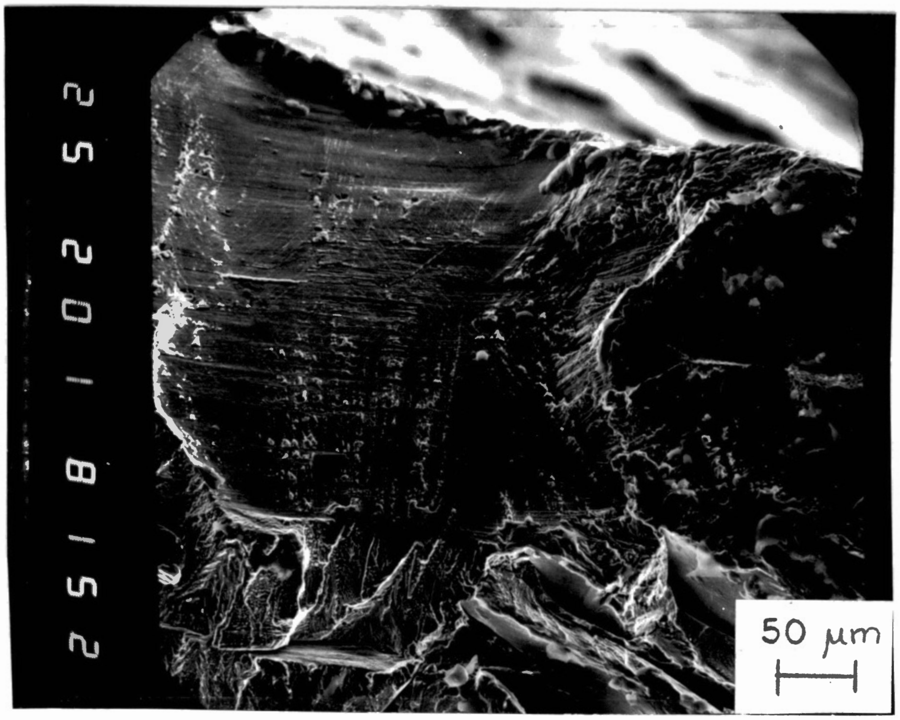
50 µm

TABLE XIV

FATIGUE LIFE DATA FOR FINE-GRAINED MONEL 400 TESTED IN AIR, HYDROGEN, AND MERCURY

Environment	Fatigue Stress, ksi	Cycles to Failure
Air	60	630,000
Hydrogen	60	79,000
Mercury	60	3,400

An interesting feature of these tests was that the fractography of the fatigue failures closely resembled tensile failures in the same environment. Striations were rarely observed on the fracture surfaces, and cracks initiated by tearing one grain deep before going to mostly intergranular in mercury and hydrogen. Air tests showed mostly transgranular tearing with a few intergranular facets scattered along the surface.

Fatigue tests run on 250 μm grain size chemically-polished samples showed much the same behavior. As shown in Table XV, a test run at 40 ksi in mercury produced a similar fatigue life to an air test run at 56 ksi, while a hydrogen test run at 56 ksi gave about one-fourth the life found in air.

The fractography of the coarse-grained fatigue samples also matched well with the tensile tests. Crack initiation was intergranular from the edge, contrasting with the fine-grained samples, in which the first grain showed transgranular tearing. Figure 40 shows the initiation zone of the mercury fatigue sample. The fracture is almost purely intergranular

TABLE XV

FATIGUE LIFE DATA FOR 250 μm GRAIN SIZE MONEL 400 TESTED IN AIR, HYDROGEN, AND MERCURY

Environment	Fatigue Stress, ksi	Cycles to Failure
Air	56	635,000
Hydrogen	56	173,000
Hydrogen	53	1,348,000
Hydrogen	50	1,900,000 (No Break)
Mercury	40	644,000

Figure 40. Initiation Zone of Fatigue Crack for Test in Mercury. The fatigue crack was nearly 100% intergranular from the edge.

Figure 41. Small Area of Tearing on Mercury Fatigue Fracture. This area covered maybe 3 to 5 grains.


50 µm

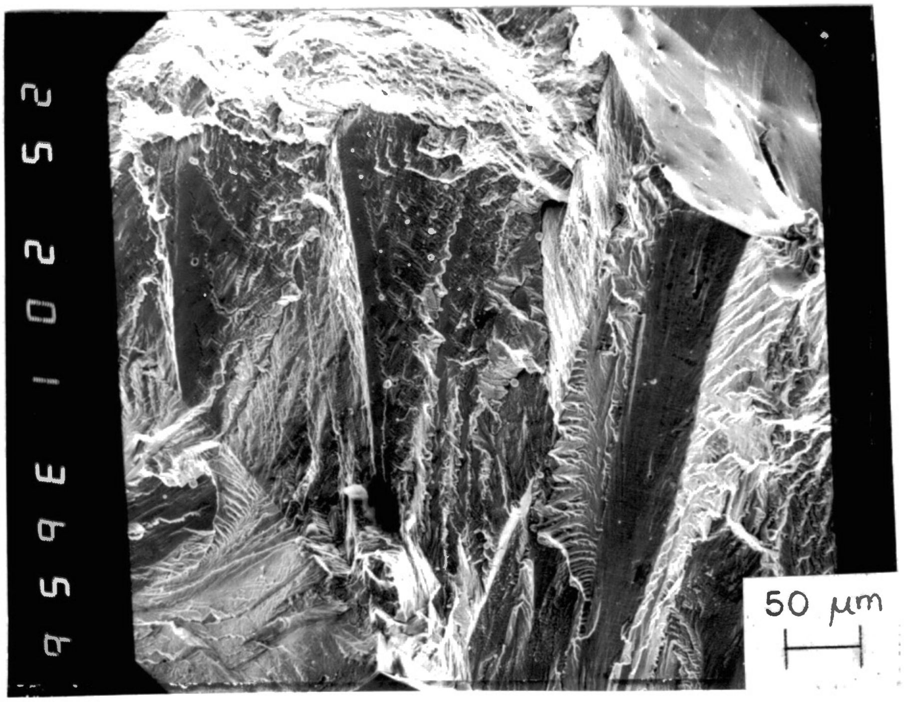
50 µm

from the edge, although a few areas could be seen where tearing occurred (Figure 41). A highly magnified area of Figure 41 is seen in Figure 42, showing extremely faint striations.

The tests in hydrogen also showed intergranular initiation zones, as seen in the 56 ksi sample (Figure 43). Tearing was seen more often than in mercury, and a transition to almost 100 percent tearing occurred only a few grains from the surface. The initiation zone of the 53 ksi test is shown in Figure 44. The crack began intergranularly at the lower right, but tearing was apparent on part of almost every grain. The 50 ksi test was interrupted at 1.9 million cycles. SZM inspection showed no cracking, so the sample was rapidly pulled to failure. Electron microscopy showed the beginnings of a crack, indicated by arrows in Figure 45. Most of the grains seen are along the side of the sample.

Discussion

Relative Embrittlement of Hydrogen and Mercury

In tensile tests with Nickel 200, Traylor [9] found that hydrogen was a somewhat more potent embrittling agent than mercury. The present tests with Monel 400 do not support that finding, as mercury consistently caused a greater loss of strength and ductility in tensile tests at a given strain rate, and gave considerably reduced fatigue lives in tests run at a given stress level. This comparative ineffectiveness of hydrogen does not seem to be a factor of limited supply of hydrogen, for Traylor found intergranular cracking at the center of Monel 400 fatigue specimens at the same hydrogen charging rate. In addition, surface cracking was observed at considerably lower stress levels in mercury than in

Figure 42. Appearance of Fatigue Striations on Mercury Fatigue Fracture. This is a highly magnified region of Figure 41. The direction of crack propagation was from bottom to top.

Figure 43. Initiation Zone of Fatigue Crack for 56 ksi Test in Hydrogen. The crack started at the lower left, and was intergranular, with some tearing in later grains.

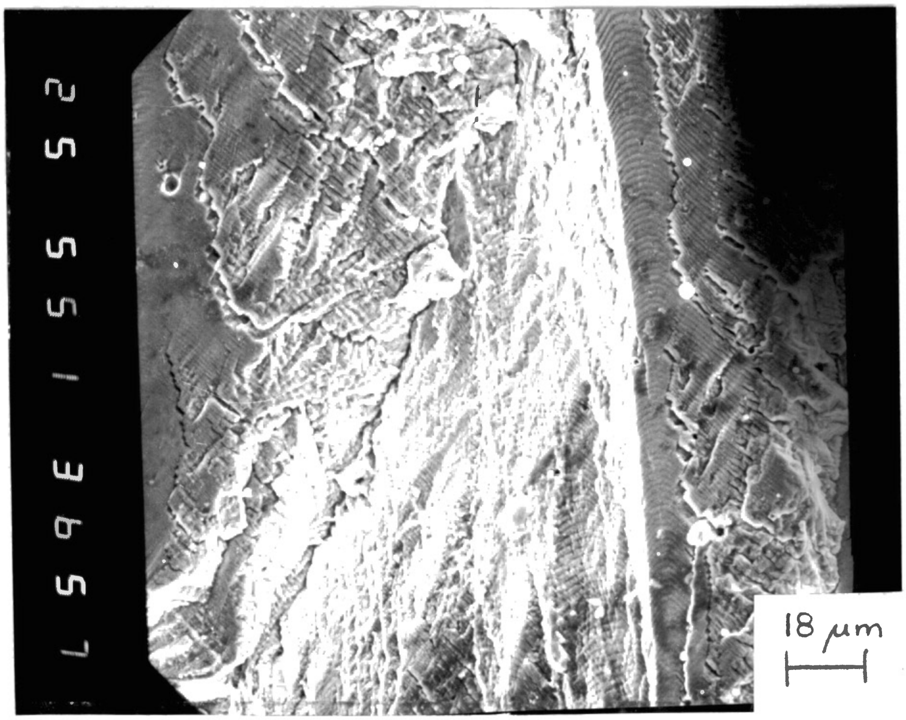
18 μm

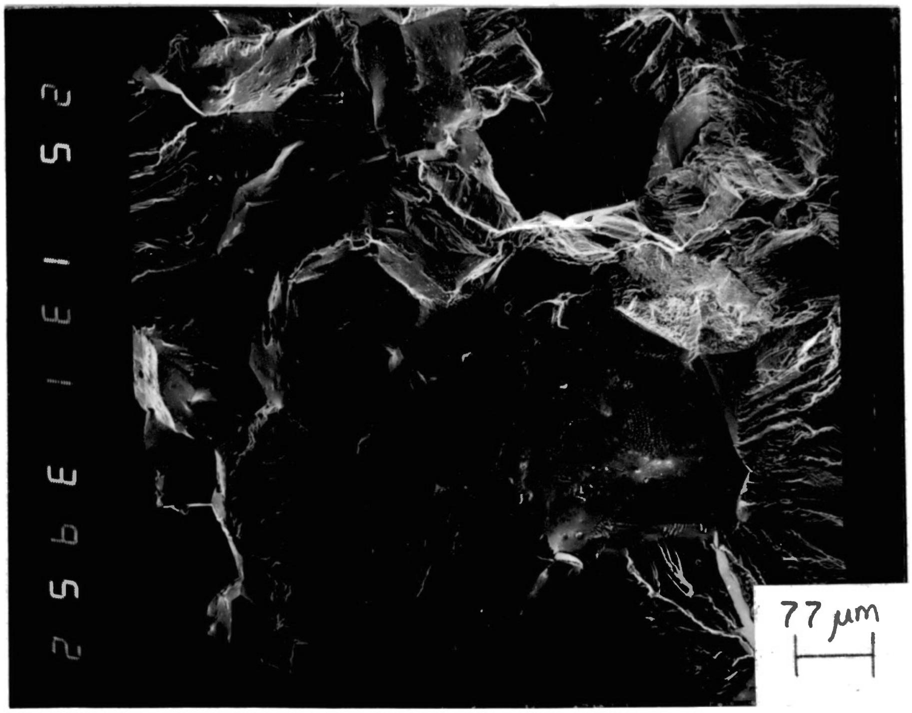
77 μm

Figure 44. Initiation Zone of Fatigue Crack for 53 ksi Test in Hydrogen. The crack began intergranularly at the bottom edge of the photograph, giving way subsequently to some mixed tearing.

Figure 45. Initiation Zone of Fatigue Crack for 50 ksi Test in Hydrogen. This test was interrupted after 1.9 million cycles and then rapidly pulled to failure. The arrows point to the initiation zone that presumably was less than one grain deep when the test was interrupted.

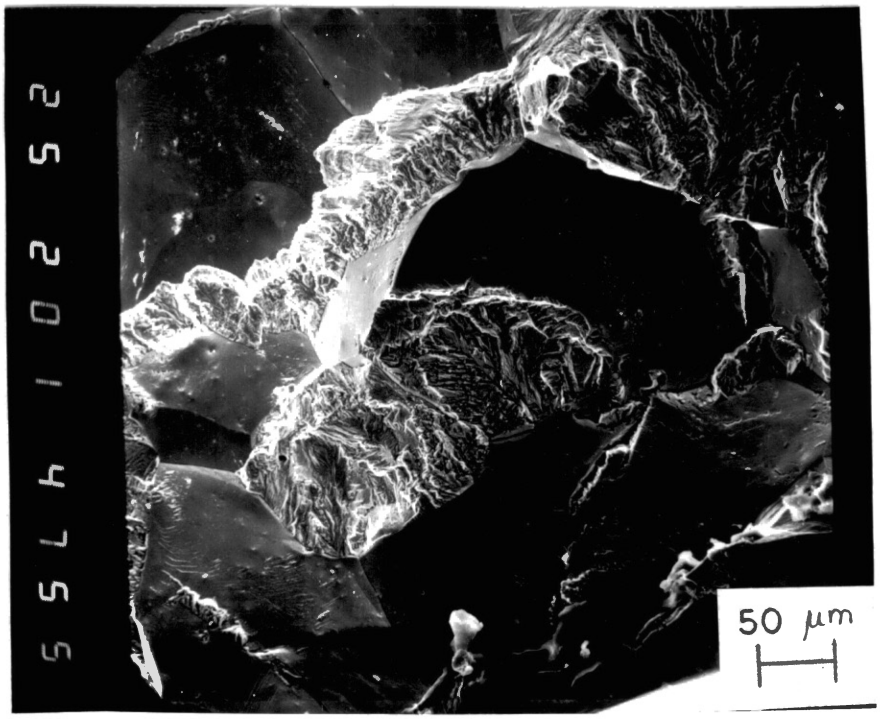
50 μm

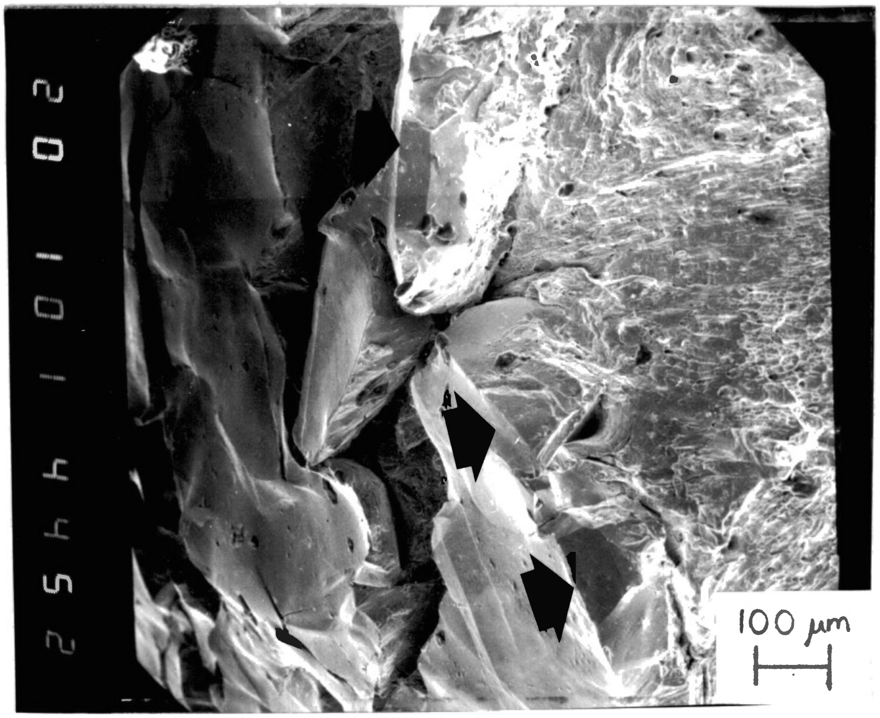
100 μm

hydrogen, though present tests have shown that an ample supply of hydrogen exists at the surface, based on tests run with different diameter specimens.

Embrittlement would seem, initially, to be a surface-dominated process. Mercury, with its large atomic size, surely cannot penetrate below the surface of the metal, and hydrogen penetration should be minimal, for the low diffusion rate (5×10^{-14} m^2/s) of hydrogen in nickel at 25°C should be of the same order of magnitude as for Monel. Depth of penetration is a function of the square root of the product of diffusivity and time [30], so the maximum penetration of hydrogen ahead of an advancing crack is ~0.5 μm [31], which seems insignificant in grain sizes from 35 to 500 μm.

A comparison can be made with hydrogen embrittlement in steels. Hydrogen can diffuse much faster into steels [32], and so cracking initiates below the surface in the plane strain zone, and breaks through to the surface at a later time. If hydrogen were penetrating significantly into Monel, similar subsurface crack initiation would be expected, which was not the case.

The inference that can be drawn is that the driving force for embrittlement, whatever it is, is stronger in mercury than in hydrogen. If an incubation period and grain boundary penetration are necessary, after Gordon and An [22], then the faster diffusion of hydrogen is more than offset by the increased potency of mercury. On the other hand, the possbility that a sufficient hydrogen concentration is unavailable--because prompt diffusion enhances dispersion--can hardly be the case, for the diffusion rate is too low.

Fracture Surface Characteristics

Comparisons of the fractography showed that the same fracture surface appearance was found in both hydrogen and mercury, though in varying degrees. The sequence was mixed intergranular/transgranular, clean intergranular, transgranular tearing, and microvoids, with a larger proportion of intergranular fracture in mercury. In tests for hydrogen embrittlement, Beachem [23] identified a sequence of intergranular, transgranular, and microvoid coalescence, which seems to be the case here. He correlated the transition in fractography with an increase in stress intensity factor, i.e., intergranular fracture at low stress intensity, going to transgranular and microvoids at higher values of stress intensity. The fact that a greater amount of intergranular fracture was found in the mercury tests points to fracture at lower stress intensities. This is consistent with the greatly reduced tensile strength, reduction in area, and fatigue life for tests in mercury. Traylor [9] found no evidence of intergranular fracture in slow tensile tests of Nickel 200 in mercury, but observed intergranular fracture in fatigue tests where the stress intensity was lower.

The stress intensity is proportional to the square root of the plastic zone radius [5]. An increase in stress intensity would therefore give increased strain around the crack tip. At some critical stress intensity, it can be argued that the plastic deformation and dislocation density reach a threshold value where specific planes of atoms within the grains become more thermodynamically active than the grain boundary atoms and therefore react preferentially. This is consistent with the results of Good [8] and Traylor [9], who demonstrated that cold worked (prestrained) materials show less intergranular embrittlement than annealed materials. In the mixed tearing zones near the surface, certain grains receive much more deformation than others by virtue of their orientation. Monel is highly anisotropic; the elastic modulus in the <111> direction is more than twice that in the <100> direction [5]. Boas and Hargreaves [33], studying coarse-grained aluminum, found that certain individual grains in tensile specimens experienced elongation seven times greater than that experienced by adjacent grains. In Monel, therefore, some grains may have already been strained beyond a certain threshold value when the crack tip reaches them, and so fail by transgranular tearing. Other, less heavily deformed grains then fail by intergranular cracking.

The concept of a threshold strain value may also explain why hydrogen causes proportionately less intergranular fracture than mercury. Tests have shown that surface cracking in hydrogen initiates at a much higher strain level than in mercury, which means that more grains may have already exceeded the threshold strain, leading to more tearing and less intergranular cracking in the hydrogen samples.

Strain Rate Effects

The FCC metals (e.g., nickel, copper, aluminum) are considered much less sensitive to variations in strain rate than the BCC metals (e.g., iron, chromium, tungsten) [5]. The following relationship has been developed to relate yield stress, σ_{ys}, to strain rate, $\dot{\varepsilon}$:

$$\sigma_{ys} = c\ \dot{\varepsilon}^{m} \qquad (2)$$

where c is a constant and m is the strain rate sensitivity. For FCC metals below about 0.5 of their melting temperature, m is quite low; at room temperature for aluminum, m equals ~0.02 [34]. For these reasons, little or no strain rate sensitivity was expected or observed for Monel 400 tested in air.

An increase in strain rate can be equated to testing at a lower temperature [5], and FCC metals show relatively small changes in yield strength over a wide range of temperatures. Annealed Monel 400, for example, has a yield strength of approximately 29 ksi at 100°C and 34 ksi at 0°C [29]. However, in the present study, a noticeable strain rate effect has been discovered in tests of Monel 400 in mercury. The large drop in tensile strength with decreasing strain rate is particularly interesting, for Funkenbusch et al. [28], Costas [27], and Traylor [9] did not associate any decrease in tensile strength with mercury embrittlement in Monel 400. Why should there be a strain rate effect associated with mercury embrittlement and, to a lesser extent, with hydrogen embrittlement? Comparisons can be made to high temperature creep. In a typical study of creep done at constant temperature; time to failure, t_f; and strain at failure, ε_f, are noted. As the stress level is raised, t_f decreases while ε_f increases. Also in creep, at high t_f and low ε_f, the fracture is intergranular; at low t_f and high ε_f, the fracture is transgranular. Creep is a thermally activated process; HE and LME may be also. There are similarities; however, without dislocation climb, in increase in stress level is needed to provide more strain. The more time taken in the slower tests provides a greater thermal contribution to enhance embrittlement. Of the current LME models, the Gordon and An [22] theory involves incubation periods and activation energies. The results already presented seem to support this model in that it correctly accounts for the effect of varying strain rate. If the embrittlement process is thermally activated, then increasing strain rates would need higher temperatures so that sufficient diffusion of the embrittler could occur. All tests in this work were run at room temperatures; hence the effect would be to decrease embrittlement at higher strain rates. As this was the observed effect, the conclusion can be drawn that the embrittlement process is thermally activated and time-dependent.

Grain Size Effects

Kamdar [17] and Gordon and An [22] proposed that in LME the fracture strength of the metal behaves according to the Petch relationship, i.e.,

$$\sigma_{\text{fracture}} \alpha \ d^{-\frac{1}{2}} \qquad (3)$$

where d is the average grain diameter. Studies of zinc bicrystals tested in liquid mercury [35] and cadmium in liquid gallium [18] confirmed this effect. Both zinc and cadmium have the hexagonal close-packed (HCP) crystal structure. A number of investigators have upheld the Petch relationship for BCC metals, which undergo the ductile-to-brittle transition [5]. The effect in FCC Monel, however, was not as pronounced. Tests in mercury showed a slight increase in embrittlement with the four finest grain sizes, but the effect was much less pronounced than that predicted by the Petch relationship. In the coarsest grain size, a marked reduction in embrittlement was noted. The extremely large grains offer little mutual constraint from plastic deformation, so the possibility exists that plane stress conditions prevail throughout the sample, hence dominating any embrittling effect. Once again, the concept of a threshold strain can be applied to explain the fractographic behavior. When the advancing crack tip meets up with a deformed grain, the existing plastic deformation is above the level which can allow intergranular fracture, so the crack propagates by tearing. In tests run in mercury, where cracking can occur at a stress level well below the tensile strength, the lack of constraint only becomes a significant factor in the extremely coarse grain size (~500 μm).

The variable grain size tests in hydrogen, as in the variable strain rate tests, showed less embrittlement than in mercury. The extent of embrittlement generally decreased with increasing grain size. As hydrogen is a less potent embrittler than mercury, a higher proportion of the tensile strength is needed to cause cracking in the presence of hydrogen. Higher stresses cause more plastic deformation. Accordingly, more grains reach the threshold strain before they see the advancing crack, even in the finer-grained samples where the mutual plastic constraint between grains is stronger. As the advancing crack contacts many more grains which have already surpassed the threshold strain level, transgranular tearing becomes the favored method of propagation. It is suggested for hydrogen that the threshold strain is surpassed much more quickly, even in the fine-grained samples, and that its effect overwhelms the embrittling effects associated with the Petch relationship. This can account for the trend of decreasing embrittlement with increasing grain size.

Fatigue Tests

In high cycle fatigue tests of engineering materials in inert environments, it is generally recognized that crack initiation makes up the overwhelming proportion of the fatigue life of a component, while fatigue crack propagation takes maybe only 1 percent of the total fatigue life

[36]. The large reduction in fatigue life for the samples tested in mercury, and the smaller reduction seen in hydrogen, point to a mechanism which stimulates initiation as well as propagation of a fatigue crack. The results show that mercury must affect the initiation considerably more than hydrogen, consistent with the tensile tests. It is interesting to note that the fractography of the fatigue tests was largely indistinguishable from that of the tensile tests. With fatigue cracks initiating at lower stress intensities, it may be anticipated that fatigue tests would show cleaner intergranular fractures than would tensile tests; this was found to be true. Also, fatigue cracks usually initiate at slip bands; this seemed to be the case for Nickel 200 in mercury [8], but the origins were intergranular here.

Static Tests

The significance of the limited tests involving hold periods under tensile load is not clear; a complete test sequence involving a range of hold times and different stress levels would be necessary to evaluate this phenomenon. This lies beyond the scope of this thesis. Presumably, some stress relaxation process is involved. The effect of the static load is similar to cold working the material, in that the slow tensile tests run after the hold periods showed less embrittlement than in the corresponding standard tensile tests. This effect of cold work was not unexpected; Price and Good [8] and Kamdar [17] have noted it in the literature.

CHAPTER V

CONCLUSIONS

1. Monel 400 is embrittled by both hydrogen and mercury, the latter being the more severe environment. Loss of ductility was accompanied by a reduction in tensile strength in both environments when compared to tests in air.

2. A common fracture sequence of intergranular, transgranular, and microvoid coalescence was identified in both environments. This sequence was associated with a constantly increasing stress intensity factor at the advancing crack tip.

3. The alloy exhibited increasing susceptibility to embrittlement with decreasing strain rate in both environments. It was felt that the driving force behind both hydrogen and mercury embrittlement is thermally activated.

4. Monel 400 showed a slight increase in embrittlement in mercury with increasing grain size, except for the coarsest-grained sample which exhibited largely ductile behavior. In hydrogen, embrittlement steadily decreased as grain size increased. Two competing processes were believed to oppositely influence the grain size effect upon embrittlement.

5. The fatigue life of the alloy was greatly reduced by mercury, and moderately reduced by hydrogen. A common embrittlement mechanism probably affected both the initiation and propagation stages of crack growth.

6. Although none of the current theories of embrittlement could fully account for the experimental observations, the results most strongly support the stress-aided diffusion penetration model of Gordon and An [22].

A SELECTED BIBLIOGRAPHY

[1] Fontana, M. G., and N. D. Greene. Corrosion Engineering. 2nd ed. New York: McGraw-Hill Book Co., Inc., 1978.

[2] Lynch, S. P. "Hydrogen Embrittlement and Liquid-Metal Embrittlement in Nickel Single Crystals." Scripta Metallurgica, 13 (1979), pp. 1051-1056.

[3] Jewett, R. P., R. J. Walter, W. T. Chandler, and R. P. Frohmberg. Hydrogen Environment Embrittlement of Metals. A NASA Technology Survey, NASA CR2163, March, 1973.

[4] Price, C. E. Personal interview. Stillwater, Oklahoma, Oct. 20, 1983.

[5] Hertzberg, R. W. Deformation and Fracture Mechanics of Engineering Materials. 2nd ed. New York: John Wiley and Sons, 1983.

[6] Culp, A. W. Principles of Energy Conversion. New York: McGraw-Hill Book Co., Inc., 1979.

[7] Tuttle, R. N., and R. D. Kane. "State-of-the-Art of H_2S Corrosion Problem Solving." Materials Performance (Jan., 1983), pp. 9-10.

[8] Price, C. E., and J. K. Good. Unpublished research. Oklahoma State University, Stillwater, Oklahoma, 1982.

[9] Traylor, L. B. "A Comparison of Hydrogen and Mercury Embrittlement of Nickel Based Alloys." (Unpub. M.S. thesis, Oklahoma State University, 1983.)

[10] Likhtman, V. I., and E. D. Shchukin. "Physico-Chemical Phenomena in the Deformation of Metals." Sov. Phys.-Uspekhi, 1 (1958), pp. 91-112.

[11] Likhtman, V. I., E. D. Shchukin, and P. A. Rebinder. Physico-Chemical Mechanics of Metals. Moscow: Academy of Science of the U.S.S.R., 1962.

[12] Rostoker, W., J. M. McCaughey, and M. Markus. Embrittlement by Liquid Metals. New York: Reinhold, 1960.

[13] Nichols, H., and W. Rostoker. "On the Mechanism of Crack Initiation in Embrittlement by Liquid Metals." Acta Metallurgica, 9 (1961), p. 504.

[14] Low, J. R. Fracture. New York: John Wiley and Sons, 1959.

[15] Robertson, W. M. "Propagation of a Crack Filled With Liquid Metal." Transactions of TME-AIME, 236 (1966), pp. 1478-1482.

[16] Westwood, A. R. C., and M. H. Kamdar. "Concerning Liquid Metal Embrittlement, Particularly of Zinc Monocrystals by Mercury." Phil. Mag., 8 (1963), pp. 787-804.

[17] Kamdar, M. H. "Embrittlement by Liquid Metals." Progress in Materials Science, 15 (1973), pp. 289-374.

[18] Stoloff, N. S., and T. L. Johnston. "Crack Propagation in a Liquid Metal Environment." Acta Metallurgica, 11 (1963), pp. 251-256.

[19] Gilman, J. J. Plasticity. Oxford: Pergamon Press, 1960.

[20] Kelly, A., W. R. Tyson, and A. H. Cottrell. "Ductile and Brittle Crystals." Phil. Mag., 15 (1967), p. 567.

[21] Krishtal, M. A. "The Formation of Dislocations in Metals on Diffusion of Surface-Active Substances in Connection With the Effect of Adsorption Embrittlement." Sov. Phys.-Doklady, 15 (1970), pp. 614-617.

[22] Gordon, P., and H. H. An. "The Mechanisms of Crack Initiation and Crack Propagation in Metal-Induced Embrittlement of Metals." Metallurgical Transactions, 13A (1982), pp. 457-472.

[23] Beachem, C. D. "A New Model for Hydrogen-Assisted Cracking." Metallurgical Transactions, 3 (1972), pp. 437-451.

[24] Zapffe, C. A. "Neumann Bands and the Planar Pressure Theory of Hydrogen Embrittlement." Journal of the Iron and Steel Institute, 154 (1946), p. 123.

[25] Tetelman, A. S., and W. D. Robertson. "The Mechanism of Hydrogen Embrittlement Observed in Iron-Silicon Single Crystals." Transactions of the AIME, 224 (1962), p. 775.

[26] Petch, N. J., and P. Stables. "Delayed Fracture of Metals Under Static Load." Nature, 169 (1952), pp. 842-843.

[27] Costas, L. P. "Effect of Phosphorus on the Embrittlement of Copper-Nickel Alloys by Mercury." Corrosion-NACE, 31 (1975), pp. 91-96.

[28] Funkenbusch, A. W., L. A. Heldt, and D. F. Stein. "The Influence of Grain Boundary Phosphorus Concentration on Liquid Metal and Hydrogen Embrittlement of Monel 400." Metallurgical Transactions, 13A (1982), pp. 611-618.

[29] Metals Handbook. 9th ed. Vol. 3. Metals Park, Ohio: ASM, 1980.

[30] Van Vlack, L. H. Elements of Materials Science and Engineering. 4th ed. Reading, Mass.: Addison-Wesley Publishing Co., Inc., 1980.

[31] Joosten, M. W., T. D. Lee, T. Goldenberg, and J. P. Hirth. "Hydrogen Effects in Metals." Third International Conference on Effect of Hydrogen on Behavior of Materials, AIME (1980), pp. 839-850.

[32] Maschino, S. E. "The Diffusion of Hydrogen in Iron and Steel." (Unpub. M.S. thesis, Oklahoma State University, 1982.)

[33] Boas, W., and M. E. Hargreaves. "On the Inhomogeneity of Plastic Deformation in the Crystals of an Aggregate." Proc. R. Soc. of London, A193 (1948), p. 89.

[34] Tegart, W. J. M. Elements of Mechanical Metallurgy. New York: The MacMillan Co., Inc., 1966.

[35] Kamdar, M. H., and A. R. C. Westwood. "Effects of Alloying on the Brittle Fracture of Zinc in Liquid Mercury." Acta Metallurgica, 16 (1968), pp. 1335-1341.

[36] Broek, D. Elementary Engineering Fracture Mechanics. The Netherlands: Sijthoff and Noordhoff International Publishers, 1978.

VITA 2

Robert Stephen Fredell

Candidate for the Degree of

Master of Science

Thesis: A DETAILED COMPARISON OF HYDROGEN AND MERCURY EMBRITTLEMENT IN MONEL 400

Major Field: Mechanical Engineering

Biographical:

Personal Data: Born in Sacramento, California, May 10, 1960, the son of Mr. and Mrs. D. P. Fredell.

Education: Graduated from Klein High School, Spring, Texas, in May, 1978; received Bachelor of Science Degree in Mechanical Engineering (Aerospace Option) from Oklahoma State University in December, 1982; completed the requirements for the Master of Science Degree at Oklahoma State University in December, 1983.

Professional Experience: Summer Roustabout, Conoco, Inc., 1979; Summer Mechanical Engineering Intern, Magnetic Peripherals, Inc., 1982; Undergraduate Teaching Assistant, Oklahoma State University, 1982; Engineer-in-Training, November, 1982.

Professional Organizations: American Society for Metals, Tau Beta Pi, Pi Tau Sigma, National Society for Professional Engineers, Oklahoma Society for Professional Engineers.